Nonreciprocal single-photon scattering in giant-spin-ensemble–waveguide magnonics

Xin Wang, Qing-Yang Qiu, Kai-Wei Huang, and Hao Xiong[*]

School of Physics, Huazhong University of Science and Technology, Wuhan 430074, China

We study nonreciprocal single-photon scattering in a giant-spin-ensemble (GSE)–waveguide magnonics system where the GSE constructed by a yttrium iron garnet sphere interacts twice with the waveguide via two separated coupling points. It is shown that the generation of nonreciprocity arises from the synergy of the breaking of time-reversal symmetry induced by the chiral coupling and the intrinsic dissipation of the magnon mode in the case of a single waveguide. The accumulated phase caused by the photon propagating between coupling points can be a powerful tool to control nonreciprocity due to quantum interference effects. Compared to the Markovian regime, single-photon transmission exhibits peculiarly nonreciprocal properties in the non-Markovian regime. Multiple narrow nonreciprocal transmission windows are observed. Non-Markovianity can break the decoupling phenomenon of the Markovian regime and non-Markovianity-induced nonreciprocity is demonstrated. We extend the study of nonreciprocity to the GSE coupled to a double-waveguide structure to explore the design of quantum devices. A high-efficiency and tunable multifrequency single-photon targeted router and circulator with narrow operational bandwidth are achieved. Our results provide an effective avenue for single-photon manipulation and have potential applications in designing magnon-based quantum devices and constructing an integrated quantum network.

I. INTRODUCTION

The waveguide quantum electrodynamics (QED) system provides an excellent platform to study quantum light-matter interactions and flexible manipulations of photons, which play important roles in quantum information processing and quantum networks [1]. Much theoretical and experimental progress has been dedicated to implement the waveguide-QED system, such as quantum dots or atoms coupled to photonic crystal waveguides or optical fibers [2,3] and superconducting qubits coupled to microwave transmission lines or resonator waveguides [4–6]. With the further development of waveguide QED, a new structure of the waveguide-emitter system was proposed, where the quantum emitter cannot be seen as a single point due to its size being comparable to or even greater than the wavelength of the waveguide modes. The dipole approximation is violated in such a situation. The atom is designed to interact with the waveguide mode via multiple points, which is the so-called giant atom, and has been experimentally demonstrated by coupling artificial superconducting qubits to bosonic modes (acoustic waves [7] or microwaves [8,9]) propagating in the waveguide. It has also been put forward that the giant atom can be created in higher dimensions by using ultracold atoms in dynamical state-dependent optical lattices [10] and be constructed in a synthetic frequency dimension [11]. Compared to a small atom system, the property of multiple coupling points of the giant atom can result in additional quantum interference effects and non-Markovian dynamics, which brings about a series of novel phenomena including frequency-dependent relaxation rates and Lamb shifts [12],

nonexponential decay [7,13,14], decoherence-free interaction [15–17], single-photon manipulation [18–21], bound states [22–24], collective radiance [25], and entanglement or disentanglement [26–28].

Recently, magnons, quanta of collective spin excitations, have attracted substantial attention and become an indispensable block for interdisciplinary studies because of their unique advantages of low dissipation, long lifetime, and excellent compatibility [29,30]. The coupling between magnons and microwave cavity photons can reach the strong and even ultrastrong regime through magnetic dipole interaction due to the large spin density in the yttrium iron garnet (YIG) sphere [31–33]. It has been demonstrated that magnons also couple to other degrees of freedom, such as optical photons [34–36], superconducting qubits [37–39], and phonons [40–43]. The delivery of coherent quantum information requires the waveguide to provide a quantum channel for carrier transport to realize remote control and integration. In the microwave frequency regime, traveling photons in the microwave waveguide can strongly couple to the magnon mode and the magnon mode can directly transfer energy or information to the waveguide by emitting a traveling photon [44–47]. Magnon-qubit dissipative coupling or magnon-cavity photons have been implemented and mediated via traveling photons of the waveguide [48,49], providing a way for non-Hermitian quantum dynamics of a hybrid magnon system. In the optical frequency regime, magnon-optical photon coupling and magnon-induced Brillouin scattering of light are observed based on an optical fiber waveguide-ferromagnet sphere system in which the YIG sphere supports two optical whispering gallery modes (WGMs) and the magnon mode, which is typically referred to as optomagnonics [34–36]. These achievements of waveguide magnonics promote the

────────
[*]haoxiong1217@gmail.com

study in the fields of the coherent conversion of optical and microwave photons [50–52], frequency combs [53–55], the remote magnon Schrödinger cat state [56], and remote magnon-magnon coupling or entanglement [57,58]. In addition, in analogy to the giant atom structure, the giant spin ensemble (GSE) has been demonstrated in experiment [59]. The GSE is constructed by a YIG sphere that supports the magnon mode and couples to traveling photons in a microwave waveguide at two well-separated coupling points. The periodic coupling and decoupling between the GSE and the waveguide can be realized. The collective behavior of two GSEs in the nested configuration is observed and their interaction can be modulated from purely coherent coupling to dissipative coupling. Thereby, the waveguide magnonics system is studied within the giant atom physics community. In comparison to the previous scheme of the giant atom constructed through superconducting qubits [7–9], the experiment of the GSE waveguide can be carried out at room temperature rather than cryogenic temperature and the GSE is an easily tunable system since the frequency of the magnon mode in a YIG sphere has wide-range adjustability via the external magnetic field [59], which offers an ideal platform for quantum information manipulation.

Chiral quantum optics provided a new route to control on-chip single-photon transport, especially nonreciprocity. Here the coupling strength between emitters and photons depends on the propagation direction and the time-reversal symmetry (TRS) of the system is broken. The chiral coupling could emerge naturally in the waveguide QED when the spin momentum locked light interacts with quantum emitters with polarization-dependent dipole transitions [60]. This has been used to control the directionality of the photon emission and realize quantum devices [61–67], e.g., single-photon diodes, targeted routers, and circulators. Recently, chirality has been introduced in giant atom physics [68–73] and chiral bound states [74] have been proposed. Meanwhile, the hybrid magnon-photon system has become a promising candidate for exploring chiral quantum interactions. On the one hand, in optomagnonics, the magnon mode unidirectionally couples to the two optical modes, which is underpinned by different selection rules for the two circulations of optical WGM photons, and finally nonreciprocal or chiral optomagnonic coupling is accomplished [34–36]. On the other hand, the chiral magnon-microwave photon interaction can be completed and modulated by tuning the positions of the magnetic (YIG) spheres inside the cavity [75,76] or waveguide [46,47,77]. These works contribute to achieve the one-way control of diverse physical phenomena and the development of magnon-based quantum devices [78–85].

In this work, we propose a scheme to realize nonreciprocal single-photon scattering in the GSE-waveguide system where the magnon mode in the GSE can couple to the waveguide with two separated coupling points. In the scenario of a single waveguide, the generation of nonreciprocity of single-photon transmission in two input directions requires not only the breaking of TRS induced by the chiral magnon-photon interaction but also the participation of the non-Hermitian potential, i.e., the intrinsic dissipation of the magnon mode. The dissipation-induced nonreciprocity [86] is realized in our work, which is similar to the system of
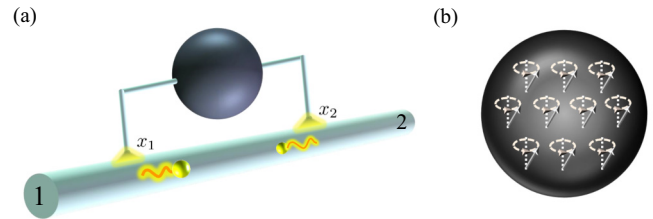

FIG. 1. (a) Schematic diagram of the GSE waveguide. A YIG sphere, which is viewed as a GSE, is coupled to the waveguide via two points with x_1 and x_2 set as $x_1 = 0$ and $x_2 = x_0$. Here the chiral magnon-photon coupling at two coupling points is considered. For simplicity, the two ports of the waveguide are labeled 1 and 2, respectively. (b) Uniform magnon excitation in the GSE (YIG sphere).

emitters asymmetrically coupled to photonic lattice [87]. In the Markovian regime, we obtain strong nonreciprocity in a window which is characterized by the Lamb shift and the effective decay rate. For the case that the GSE decouples to the waveguide in the Markovian regime, the single-photon transmission is always reciprocal. In the non-Markovian regime, non-Markovianity can break the decoupling phenomenon and produces strong nonreciprocity of multiple frequency points. Thus, non-Markovianity-induced nonreciprocity is observed [68,73]. For other cases, non-Markovianity can extend a nonreciprocal window to multiple strongly nonreciprocal windows; thus non-Markovianity can enhance nonreciprocity. In the case of two waveguides, a multifrequency single-photon targeted router and circulator with properties including high efficiency, strong tunability, and narrow operational bandwidth are implemented. Compared to the previous scheme of the GSE waveguide [59], we extend it to chiral coupling, the non-Markovian regime, and the GSE–double-waveguide structure. We prove that it is completely possible to achieve nonreciprocity, non-Markovian properties, and magnon-based quantum devices in the GSE-waveguide system. Our results may provide inspiration for integrating magnons in quantum information.

II. NONRECIPROCAL SINGLE-PHOTON TRANSMISSION BASED ON THE CHIRAL GIANT-SPIN-ENSEMBLE–WAVEGUIDE SYSTEM

As intuitively displayed in Fig. 1, we consider a GSE-waveguide system which has been experimentally realized based on the YIG sphere interacting with the meandering microwave microstrip waveguide [59]. The YIG sphere is viewed as the GSE because it can be coupled to the waveguide by two points with $x_1 = 0$ and $x_2 = x_0$. We explore nonreciprocity by applying chiral magnon-photon coupling at two coupling points. The total Hamiltonian of the system can be expressed as $H = H_{\mathrm{wg}} + H_{\mathrm{m}} + H_{\mathrm{int}}$, in which H_{wg}, H_{m}, and H_{int} are the Hamiltonian of the waveguide, the magnon mode in the GSE, and the GSE-waveguide interaction, respectively. They can be given by ($\hbar = 1$) [59,88,89]

$$H_{\mathrm{wg}} = -iv_g \int dx \left(C_r^\dagger(x) \frac{\partial}{\partial x} C_r(x) - C_l^\dagger(x) \frac{\partial}{\partial x} C_l(x) \right), \quad (1)$$

$$H_{\mathrm{m}} = (\omega_m - i\gamma_m)m^{\dagger}m, \qquad (2)$$

$$
\begin{aligned}
H_{\mathrm{int}} = \int dx \{ &\delta(x)[g_r C_r^{\dagger}(x)m + g_l C_l^{\dagger}(x)m] \\
&+ \delta(x - x_0)[g_r C_r^{\dagger}(x)m + g_l C_l^{\dagger}(x)m] + \mathrm{H.c.}\}.
\end{aligned} \qquad (3)
$$

Here $C_r^{\dagger}(x)$ $[C_l^{\dagger}(x)]$ is creation operator of the right (left) propagation photon in the waveguide, v_g denotes group velocity of the photon, $m^{\dagger}$ is creation operator of the magnon mode, and ω_m and γ_m are the magnonic frequency and intrinsic dissipation rate, respectively [59,90,91]. The magnon mode is coupled to the right- or left-moving photon in the waveguide with the coupling strength g_r or g_l. The Dirac functions $\delta(x)$ and $\delta(x - x_0)$ imply that the magnon-waveguide interactions occur at $x = 0$ and $x = x_0$, respectively. The eigenstate of the system in single-excitation subspace can be written as

$$|\Psi\rangle = \int dx[\Phi_r(x)C_r^{\dagger}(x) + \Phi_l(x)C_l^{\dagger}(x)]|\varnothing\rangle + u_m m^{\dagger}|\varnothing\rangle, \qquad (4)$$

where $|\varnothing\rangle$ is the vacuum, $\Phi_r(x)$ $[\Phi_l(x)]$ represents the wave function of photon moving in the right (left) direction, and u_m is the excitation amplitude of the magnon mode.

By solving the steady-state Schrödinger equation $H|\Psi\rangle = \omega|\Psi\rangle$ based on Eqs. (1)–(4), we can obtain the equations

$$-iv_g\frac{\partial}{\partial x}\Phi_r(x) + g_r u_m[\delta(x) + \delta(x - x_0)] = \omega\Phi_r(x), \qquad (5)$$

$$iv_g\frac{\partial}{\partial x}\Phi_l(x) + g_l u_m[\delta(x) + \delta(x - x_0)] = \omega\Phi_l(x), \qquad (6)$$

$$
\begin{aligned}
(\omega_m - i\gamma_m)u_m &+ g_r[\Phi_r(0) + \Phi_r(x_0)] \\
&+ g_l[\Phi_l(0) + \Phi_l(x_0)] = \omega u_m,
\end{aligned} \qquad (7)
$$

where ω is the frequency of a single photon and satisfies the linear dispersion relation $\omega = kv_g$. When a single photon with wave vector k is input from port 1 (P_1) of the waveguide, a single-photon wave function in the right or left direction [88,89] $\Phi_r(x) = e^{ikx}[\Theta(-x) + A\Theta(x)\Theta(x_0 - x) + t_{1\to2}\Theta(x - x_0)]$ or $\Phi_l(x) = e^{-ikx}[t_{1\to1}\Theta(-x) + B\Theta(x)\Theta(x_0 - x)]$, respectively, can be constructed. For the case of single-photon input from port 2 (P_2), they take the forms $\Phi_r(x) = e^{ikx}[t_{2\to2}\Theta(x - x_0) + \tilde{A}\Theta(x)\Theta(x_0 - x)]$ and $\Phi_l(x) = e^{-ikx}[\Theta(x - x_0) + \tilde{B}\Theta(x)\Theta(x_0 - x) + t_{2\to1}\Theta(-x)]$, where $\Theta(x)$ is the Heaviside step function, with $\Theta(0) = \frac{1}{2}$, $\Theta(x > 0) = 1$, and $\Theta(x < 0) = 0$; A and $t_{1\to2}$ denote the transmission amplitudes in the regions $0 < x < x_0$ and $x > x_0$, respectively, for the case of photon input from P_1; and $t_{1\to1}$ and B are reflection amplitudes in the regions $x < 0$ and $0 < x < x_0$, respectively. For the case of a photon input from P_2, $\tilde{A}$ and $\tilde{B}$ are defined as reflection and transmission amplitudes, respectively, in the region of $0 < x < x_0$. In addition, $t_{2\to1}$ and $t_{2\to2}$ are transmission and reflection amplitudes in the regions of $x < 0$ and $x > x_0$, respectively. Substituting the above expressions of $\Phi_r(x)$ and $\Phi_l(x)$ into Eqs. (5)–(7), the corresponding transmission amplitudes can be obtained

$$t_{1\to2} = \frac{\tilde{\Delta} + i[\Gamma_l(1 + e^{i\theta}) - \Gamma_r(1 + e^{-i\theta})]}{\tilde{\Delta} + i(\Gamma_l + \Gamma_r)(1 + e^{i\theta})}, \qquad (8)$$

$$t_{2\to1} = \frac{\tilde{\Delta} + i[-\Gamma_l(1 + e^{-i\theta}) + \Gamma_r(1 + e^{i\theta})]}{\tilde{\Delta} + i(\Gamma_l + \Gamma_r)(1 + e^{i\theta})}. \qquad (9)$$

Here $\tilde{\Delta} = \Delta + i\gamma_m$ with the detuning $\Delta = \omega - \omega_m$ between the magnon mode and incident photon, $\Gamma_{l/r} = g_{l/r}^2/v_g$ is the radiative damping rate of the magnon mode emitted into the waveguide in the left or right direction, and $\theta = kx_0$ represents the accumulated phase of the photon moving between two coupling points. Through the expressions $\Delta = \omega - \omega_m$ and $\omega = kv_g$, the phase θ can be rewritten as $\theta = \theta_0 + \tau\Delta$ with the corresponding propagating time $\tau = x_0/v_g$ and the constant part $\theta_0 = \omega_m x_0/v_g$. It is worth pointing out that the frequency ω_m of the magnon mode is linearly proportional to the external magnetic field H, i.e., $\omega_m = \gamma H$, with $\gamma/2\pi = 28$ GHz/T the gyromagnetic ratio [59]. Therefore, the phase θ_0 can be modulated flexibly by the external magnetic field. Furthermore, the experiment with the GSE waveguide can be carried out at room temperature since the interaction of the magnon mode in the GSE and the microwave photon mode in the waveguide will not be affected by the thermal excitations even at room temperature [59]. These demonstrate the superiority of the GSE system. The distance of two coupling points x_0 is also a mean to adjust the phase θ and it brings about the variation of propagating time τ. When τ is small enough to be safely ignored, the system is in the Markovian regime. For the case of a large enough coupling distance x_0 in which time τ cannot be ignored, the system enters the so-called non-Markovian regime. In the following, we will discuss nonreciprocal single-photon transmission properties of the GSE-waveguide system in both the Markovian and non-Markovian regimes.

A. Markovian regime

In the Markovian regime, the propagating time τ satisfies $\tau\Gamma_{l/r} \ll 1$ [7,13,14,59]; thus the term $\tau\Delta$ in the expression of the phase θ can be safely neglected. Under this condition, the phase θ can be replaced by θ_0. In order to study the property of single-photon transmission, the transmission probabilities of different input directions $T_{1\to2} = |t_{1\to2}|^2$ and $T_{2\to1} = |t_{2\to1}|^2$ are introduced. Meanwhile, we define the isolation depth $I = |T_{1\to2} - T_{2\to1}|$ to characterize nonreciprocity of single-photon transmission. We consider the chiral GSE-waveguide system where the magnon mode can be coupled to a propagating photon with different strength for different propagating directions, whose realization may be inspired by previous chiral magnon-photon schemes [46,47,75–77,90,92] and our proposed effective scheme of the chiral GSE waveguide in Appendix B. The chiral coupling of the magnon photon $g_l \neq g_r$, i.e., $\Gamma_l \neq \Gamma_r$, is considered and it further causes the breaking of the TRS of the system, which will bring about the generation of nonreciprocity. In our work, we achieve the nonreciprocal single-photon scattering through this chiral mechanism.

Figure 2 shows the nonreciprocal property of single-photon transmission. We plot $T_{1\to2}$, $T_{2\to1}$, and I varying with Δ and θ_0 in Figs. 2(a)–2(c), respectively. Obviously, for different input directions, single-photon transmission properties can be different and have a strong dependence on the phase θ_0, which exhibits that the nonreciprocity is realized and it has strong
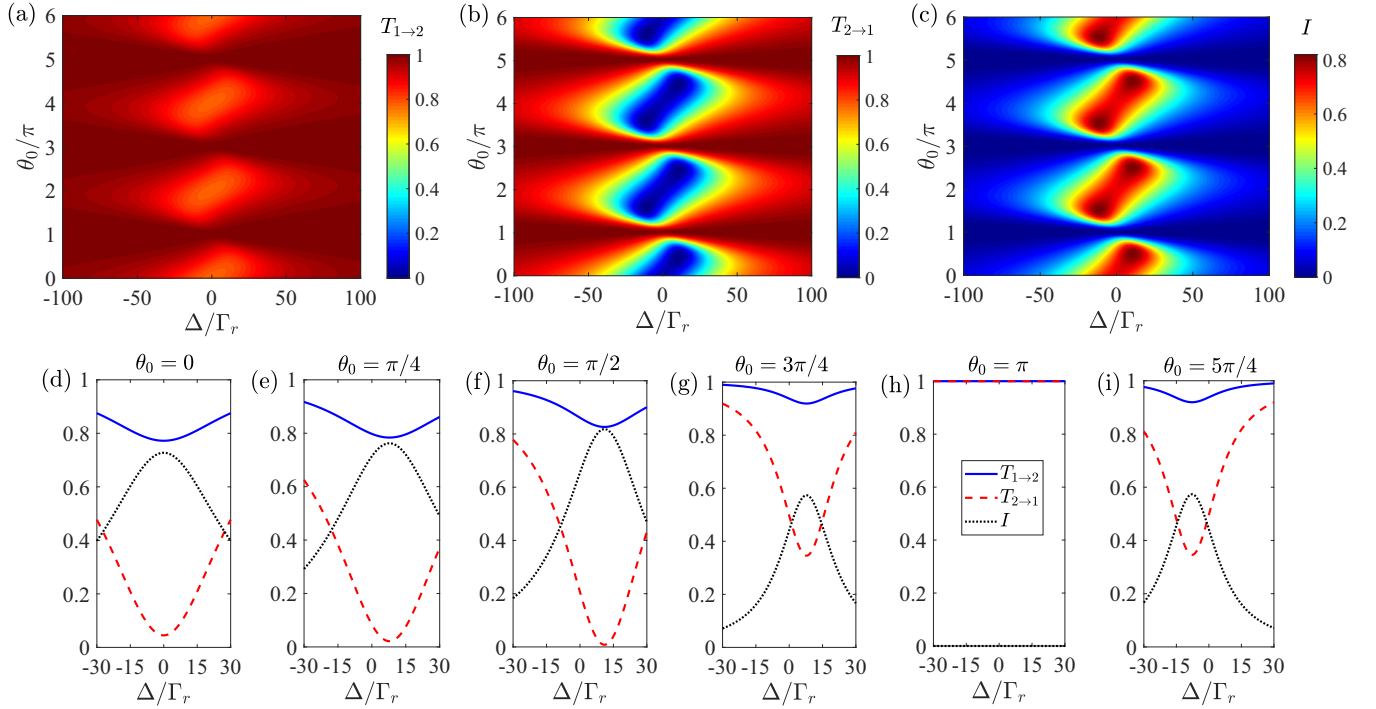
FIG. 2. (a) Transmission probability $T_{1\rightarrow2}$ from port 1 to port 2, (b) transmission probability $T_{2\rightarrow1}$ from port 2 to port 1, and (c) isolation depth I varying with Δ and θ_0. (d)–(i) Plots of $T_{1\rightarrow2}$, $T_{2\rightarrow1}$, and I versus Δ for different values of θ_0. The other parameters are $\Gamma_l = 10\Gamma_r$ and $\gamma_m = 11\Gamma_r$.

tunability. We find that the strength of nonreciprocity, i.e., isolation depth I, can reach a maximum for $\theta_0 = (\frac{1}{2} + \xi)\pi$ (ξ is integer) and a minimum ($I = 0$) for $\theta_0 = (2\xi + 1)\pi$. This is because the constructive interference between emissions from two coupling points occurs when $\theta_0 = (\frac{1}{2} + \xi)\pi$. However, for $\theta_0 = (2\xi + 1)\pi$, the magnon mode is obscured and decoupled to the waveguide due to the destructive interference, which is consistent with the recent experiment for the GSE waveguide [59]. In this situation $T_{1\rightarrow2} = 1$ and $T_{2\rightarrow1} = 1$, so the transmission is always reciprocal. The periodic interference could cause the GSE to couple and decouple with the waveguide. Thus, the nonreciprocity of single-photon transmission can be modulated periodically. In addition, the phase θ_0 can be used to regulate the frequency position of the optimal nonreciprocity and the operational bandwidth of the nonreciprocity, as shown in Figs. 2(d)–2(i). The phase-dependent effective detuning $\Delta_{\text{eff}} = \Delta - \Delta_L$ and decay rate $\Gamma_{\text{eff}} = \gamma_m + (\Gamma_l + \Gamma_r)(1 + \cos\theta_0)$ can be obtained based on Eq. (8) or (9). Here $\Delta_L = (\Gamma_l + \Gamma_r)\sin\theta_0$ is the Lamb shift induced by the GSE. In addition, $T_{1\rightarrow2}$ and $T_{2\rightarrow1}$ reach a minimum value at the effective resonance point $\Delta = \Delta_L$ (i.e., $\Delta_{\text{eff}} = 0$), which brings about the maximum value of I and the phase-modulated frequency position of optimal nonreciprocity. The full width at half maximum is described by Γ_{eff}. Thus, one can choose the appropriate value of θ_0 to obtain the desired operational bandwidth of the high level of isolation depth single-photon transmission.

Furthermore, the physical mechanism of nonreciprocal transmission can also be understood by the magnon excitation for different input directions. The amplitudes of magnon excitations $u_{m1\rightarrow2}$ and $u_{m2\rightarrow1}$ are obtained through solving Eqs. (5)–(7), which corresponds to the situation of the photon

input from P_1 and P_2, respectively. They are represented as

$$u_{m1\rightarrow2} = \frac{g_r(1 + e^{i\theta})}{\tilde{\Delta} + i(\Gamma_l + \Gamma_r)(1 + e^{i\theta})}, \tag{10}$$

$$u_{m2\rightarrow1} = \frac{g_l e^{-i\theta}(1 + e^{i\theta})}{\tilde{\Delta} + i(\Gamma_l + \Gamma_r)(1 + e^{i\theta})}. \tag{11}$$

The magnon excitation spectrum can be defined as [89] $M_{1\rightarrow2} = |u_{m1\rightarrow2}|^2/v_g$ and $M_{2\rightarrow1} = |u_{m2\rightarrow1}|^2/v_g$. From Figs. 3(a) and 3(b) we can observe that $M_{1\rightarrow2}$ is markedly suppressed and $M_{2\rightarrow1}$ is greatly enhanced under the condition of chiral coupling compared to nonchiral coupling. This indicates the occurrence of nonreciprocal photon absorbtion based on chiral coupling. Therefore, single-photon transmission spectra display the nonreciprocal characteristic in two different input directions. Meanwhile, we define the difference $\Delta_M = |M_{1\rightarrow2} - M_{2\rightarrow1}|$ of the magnon excitation
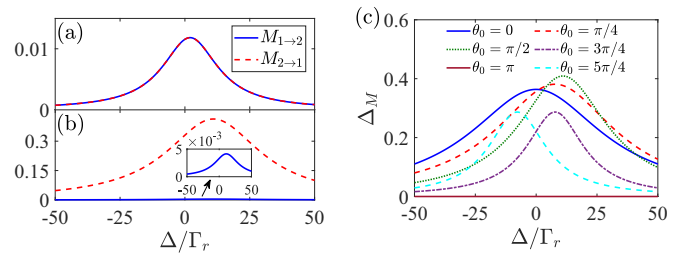

FIG. 3. Magnon excitation spectra $M_{1\rightarrow2}$ and $M_{2\rightarrow1}$ for different input directions versus Δ when $\theta_0 = \pi/2$ for (a) nonchiral coupling $\Gamma_l = \Gamma_r$ and (b) chiral coupling $\Gamma_l = 10\Gamma_r$. (c) Asymmetric magnon responses Δ_M versus Δ for the different values of phase θ_0. The other parameters are the same as in Fig. 2.
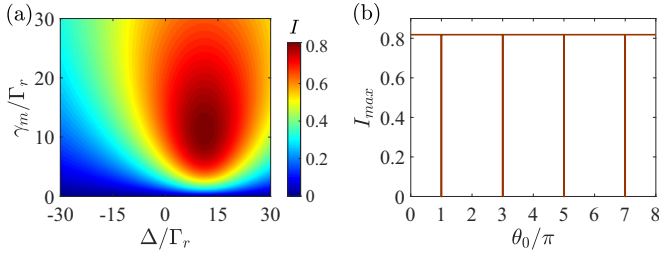
FIG. 4. (a) Isolation depth I varying with Δ and γ_m when $\theta_0 = \pi/2$. (b) Maximum value $I_{\max}$ of the isolation depth versus θ_0 with $\gamma_m = (\Gamma_l + \Gamma_r)(1 + \cos\theta_0)$. The other parameters are the same as in Fig. 2.

FIG. 5. (a) Shown on top is the isolation depth I versus chiral rate η, for $\Delta = 0$ and $\theta_0 = \pi/2$, and the maximum value $I_{\max}$ of the isolation depth versus η. The bottom plot shows the asymmetric magnon responses Δ_M versus chiral rate η. (b) Plot of I varying with Δ and θ_0 for $\Gamma_l = 0$. The insets show $T_{1\rightarrow2}$, $T_{2\rightarrow1}$, and I versus Δ for $\theta_0 = \pi/2$ (right) and $\theta_0 = 5\pi$ (left). Here $\gamma_m = (\Gamma_l + \Gamma_r)(1 + \cos\theta_0)$.

probabilities of two directions to describe the degree of asymmetric magnon responses and it is plotted as a function of Δ for different values of θ_0 in Fig. 3(c). The optimal frequency position and linewidth of asymmetric magnon responses Δ_M can be changed via the phase θ_0, which allows us to regulate the nonreciprocity of the system through θ_0.

The intrinsic dissipation of the magnon mode plays an important role in generating nonreciprocity in our scheme. The isolation depth I varying with the detuning Δ and the dissipation γ_m is exhibited in Fig. 4(a). For $\gamma_m = 0$, $I = 0$. Thus, in the absence of dissipation, single-photon transmission is reciprocal even in the chiral condition corresponding to TSR breaking. When the dissipation is taken into account ($\gamma_m \neq 0$), the nonreciprocity can be completed. We can understand this phenomenon through comparing Eqs. (8) and (9). The transmission probabilities $T_{1\rightarrow2}$ and $T_{2\rightarrow1}$ have the same denominator and their numerators can be rewritten as $[\Delta - \sin\theta_0(\Gamma_r + \Gamma_l)]^2 + [\gamma_m + (\Gamma_l - \Gamma_r)(1 + \cos\theta_0)]^2$ and $[\Delta - \sin\theta_0(\Gamma_r + \Gamma_l)]^2 + [\gamma_m + (\Gamma_r - \Gamma_l)(1 + \cos\theta_0)]^2$, respectively. This clearly shows that the nonreciprocity arises from the dissipation γ_m and the chiral coupling $\Gamma_l \neq \Gamma_r$. From another perspective, the GSE can be viewed as a scattering center in our work [93]. When the non-Hermitian potential is introduced ($\gamma_m \neq 0$), the dissipation into the environment endows the system with an intrinsic direction-dependent asymmetry. As a result, the synergy of the non-Hermitian property and TSR breaking results in nonreciprocity of scattering. This is similar to dissipation-induced nonreciprocity [86,87]. In addition, one can observe from Fig. 4(a) that the maximum value of I can be more than 0.8 when $\gamma_m = 11\Gamma_r$. This is because the strongest nonreciprocity can be realized at $\Delta = \Delta_L$ and $\gamma_m = (\Gamma_l + \Gamma_r)(1 + \cos\theta_0)$. In addition, $I_{\max} = |(\Gamma_l^2 - \Gamma_r^2)/(\Gamma_l + \Gamma_r)^2|$ if $\theta_0 \neq (2\xi + 1)\pi$. In this case, $I_{\max}$ in the whole frequency range can be a fixed value independent of θ_0 except for $\theta_0 = (2\xi + 1)\pi$, as shown in Fig. 4(b).

Through the above analysis, the maximum value of I cannot be improved by θ_0 and γ_m; however, it significantly depends on Γ_l and Γ_r. Here we define the chiral rate $\eta = \Gamma_l/\Gamma_r$ to study the influence of chirality on nonreciprocity. The isolation depth I for a special frequency photon $\omega = \omega_m$ and $I_{\max}$ versus η are plotted in Fig. 5(a). The nonreciprocity can be turn on or off by the chiral rate η because the magnon responses in the two input directions are symmetric or asymmetric. In particular, for the case of $\eta = 1$, which corresponds
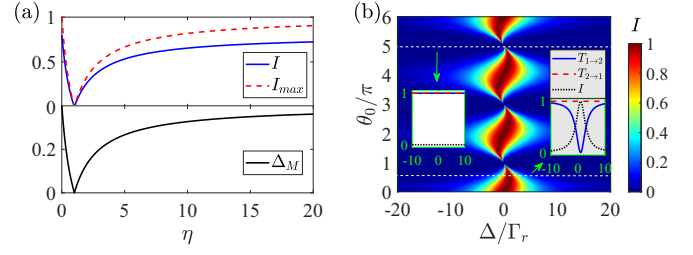
to the nonchiral coupling, $\Delta_M = 0$ due to same magnon responses $M_{1\rightarrow2} = M_{2\rightarrow1}$. Thus, nonreciprocal single-photon transmission is turned off. When $\eta = 0$, which corresponds to the perfect chiral coupling, i.e., $\Gamma_l = 0$ and $\Gamma_r \neq 0$. In this case, $T_{2\rightarrow1} \equiv 1$ since the incident single photon decouples to the GSE; however, $T_{1\rightarrow2}$ can be reach 0 for optimal system parameters and the perfect nonreciprocity $I_{\max} = 1$ is realized [see Fig. 5(b)]. The single-photon diode behavior is actually accomplished based on the GSE system. Meanwhile, the nonreciprocity still be shut down for $\theta_0 = (2\xi + 1)\pi$. Thus, the phase θ_0 can be used as a switch of the single-photon diode.

B. Non-Markovian regime

In this section we study the nonreciprocity of single-photon transmission in the non-Markovian regime, where the propagating time τ cannot be negligible, so the phase shift $\theta = \theta_0 + \tau\Delta$ depends on the detuning Δ. Similar to the giant atom system [7,13,14], the non-Markovian effect should be considered when the separation x_0 between the two coupling points of the GSE-waveguide interaction is large enough.

We plot the transmission spectra of different input directions as a function of Δ in Fig. 6(a) for the case of nonchiral coupling. When the Markovian approximation is broken, single-photon transmission displays a more complex structure. For any input direction, the phenomenon of multiple absorbtion dips or transmission peaks appears in the output spectra. Therefore, we extend the experimental system in Ref. [59] to the non-Markovian regime and predict that the non-Markovian characteristic can be realized in the GSE-waveguide system. This is similar to the time-delayed quantum coherent feedback [94,95] in which the quantum coherent output is fed back into the system after the time delay and each feedback is regraded as the input interacts with the system again; the interference effect causes output spectra to have the multiple transparency windows. In present work, the bidirectional propagating waves in the scatting interval (the region between two coupling points) interact with the GSE multiple times, which can be confirmed based on the magnon excitation spectra, as shown in Fig. 6(b). This further induces high-order scattering processes. The interference of the bidirectional propagating waves gives rise to the formation of multiple transparency windows in the GSE system. However,
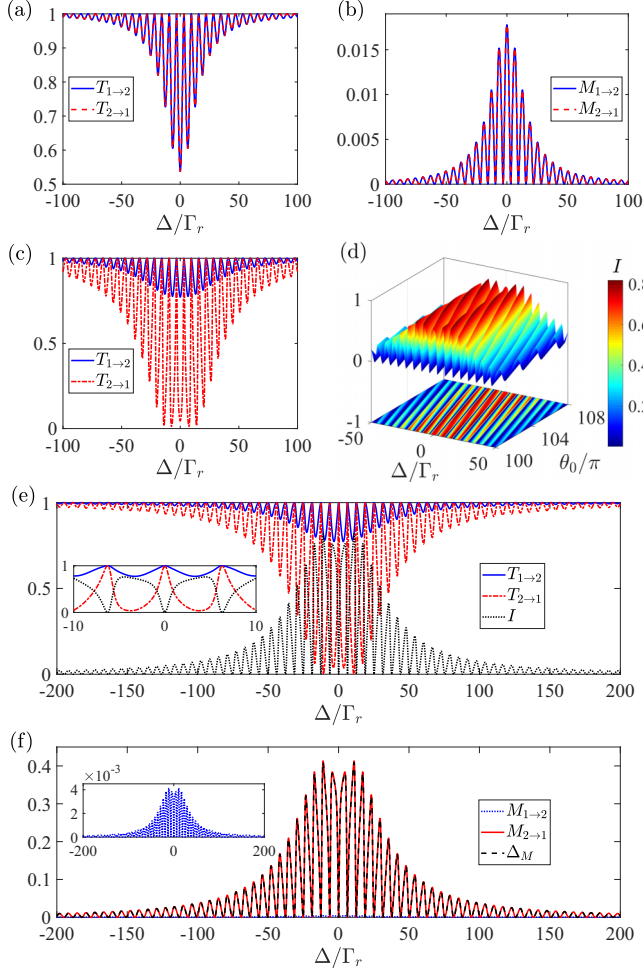
FIG. 6. (a) Transmission probability $T_{1\to2}$ from port 1 to port 2 and transmission probability $T_{2\to1}$ from port 2 to port 1 and (b) magnon excitation spectra $M_{1\to2}$ and $M_{2\to1}$ versus Δ for nonchiral coupling when $\theta_0 = 100\pi$. (c) Plot of $T_{1\to2}$ and $T_{2\to1}$ versus Δ for chiral coupling for $\theta_0 = 100\pi$. (d) Isolation depth I varying with Δ and θ_0. (e) Plot of $T_{1\to2}$, $T_{2\to1}$, and I versus Δ for $\theta_0 = 105\pi$. (f) Plot of $M_{1\to2}$, $M_{2\to1}$, and Δ_M versus Δ for $\theta_0 = 105\pi$. In (c)–(f) $\Gamma_l = 10\Gamma_r$. In addition, $\tau\Gamma_r = 1$ and the other parameters are the same as in Fig. 2.

the single-photon transmission remains reciprocal due to the TRS under the nonchiral condition.

For the chiral coupling situation, the transmission spectra of two different input directions are plotted in Fig. 6(c). They have the same oscillation tendency, but transmission probability is enhanced in one direction and restrained in the opposite, which suggests that strong nonreciprocity can still be achieved in the non-Markovian regime and extended to multiple frequency points. In addition, from Fig. 6(d) one can find that various frequency point values satisfying a high level of isolation depth I are achieved by regulating the phase θ_0. In particular, in the non-Markovian regime, the GSE is no longer decoupled to the waveguide and the asymmetric magnon responses occur even in the condition of $\theta_0 = (2\xi + 1)\pi$ [see Fig. 6(f)]. This further results in nonreciprocity rather than reciprocity when $\theta_0 = (2\xi + 1)\pi$ [see Fig. 6(e)]. Such a phenomenon does not exist in the Markovian regime
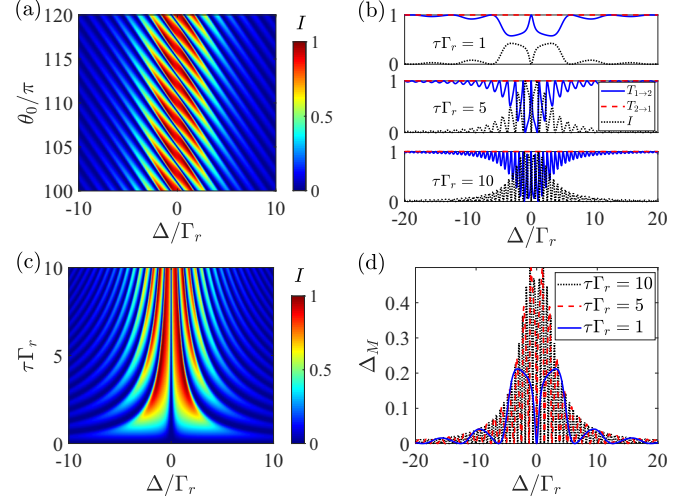

FIG. 7. (a) Isolation depth I varying with Δ and θ_0 for $\tau\Gamma_r = 5$. (b) Transmission probability $T_{1\to2}$ from port 1 to port 2, transmission probability $T_{2\to1}$ from port 2 to port 1, and isolation depth I versus Δ. (c) Isolation depth I varying with Δ and τ. (d) Asymmetric magnon response Δ_M versus Δ for different values of $\tau\Gamma_r$. In (b)–(d) $\theta_0 = 105\pi$. In addition, $\Gamma_l = 0$ and $\gamma_m = \Gamma_r$.

[see Fig. 2(h)] and so it is called non-Markovianity-induced nonreciprocity [68,73]. For $\theta_0 \neq (2\xi + 1)\pi$, non-Markovianity can extend a nonreciprocal window to multiple strongly nonreciprocal windows, which is referred to as non-Markovianity enhanced nonreciprocity. When the system is under the condition of perfect chiral coupling [Fig. 7(a)], we can obtain perfect single-photon nonreciprocal transmission at multiple frequency points. In addition, when $\theta_0 = (2\xi + 1)\pi$, non-Markovianity-induced nonreciprocity can be perfect. This is because the single-photon input from P_2 cannot be coupled to the GSE and is output directly from P_1. However, single-photon input from P_1 can interact with the GSE for $\theta_0 = (2\xi + 1)\pi$ and the value of $T_{1\to2}$ can be suppressed gradually to 0 with more frequency points with the increase of τ [see Fig. 7(b)]. Thus, by increasing the delay time τ, the isolation depth I can be enhanced. The peaks of perfect nonreciprocity ($I = 1$) get closer to $\Delta = 0$ and get sharper with the enhancement of τ, which indicates that the nonreciprocal transmission spectrum oscillates faster and the perfect nonreciprocity can work well at more frequency points, as shown in Fig. 7(c). This phenomenon occurs because the interaction between the GSE and waveguide presents a time dependence. The non-Markovian-induced asymmetric magnon response is produced for $\theta_0 = (2\xi + 1)\pi$ and it gets stronger and oscillates faster when τ is enhanced, as shown in Fig. 7(d). Thus, we can get a more refined spectrum of perfect nonreciprocity and realize a multifrequency narrow-bandwidth single-photon diode.

III. SINGLE-PHOTON TARGETED ROUTER AND CIRCULATOR

In this section we explore the possibility of realizing a quantum device including a single-photon targeted router and circulator [61–63] based on the GSE, which may be-
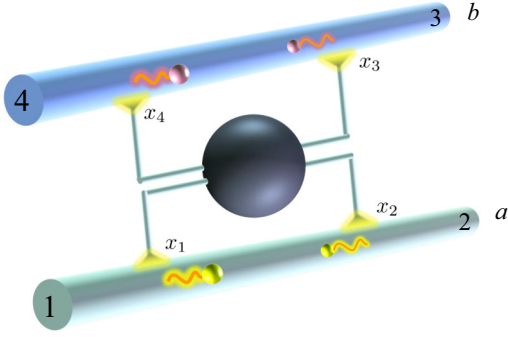
FIG. 8. Schematic diagram of the GSE coupled to two microwave waveguides labeled a and b. The GSE is coupled to each waveguide with two coupling points at x_1 and x_2 and at x_3 and x_4, respectively. The four ports are labeled 1, 2, 3, and 4, respectively.

come the key elements for quantum information processing in scalable integrated magnon-based quantum network [29,30]. We consider a GSE–double-waveguide system in which the GSE couples to each waveguide with two coupling points. We set the same distance between the two coupling points of each waveguide, i.e., the coupling positions are located at $x_1 = x_4 = 0$ and $x_2 = x_3 = x_0$. For the sake of discussion, the four ports of double waveguides are labeled 1, 2, 3, and 4, as described in Fig. 8. The Hamiltonian of system can be written as

$$H_{\mathrm{wg}} = -iv_g \int dx \left(C_{ra}^\dagger(x)\frac{\partial}{\partial x}C_{ra}(x) - C_{la}^\dagger(x)\frac{\partial}{\partial x}C_{la}(x) \right)$$
$$- iv_g \int dx \left(C_{rb}^\dagger(x)\frac{\partial}{\partial x}C_{rb}(x) - C_{lb}^\dagger(x)\frac{\partial}{\partial x}C_{lb}(x) \right),$$
(12)

$$H_{\mathrm{m}} = (\omega_m - i\gamma_m)m^\dagger m,$$
(13)

$$H_{\mathrm{int}} = \int dx\{\delta(x)[g_{ra}C_{ra}^\dagger(x)m + g_{la}C_{la}^\dagger(x)m$$
$$+ g_{rb}C_{rb}^\dagger(x)m + g_{lb}C_{lb}^\dagger(x)m]$$
$$+ \delta(x - x_0)[g_{ra}C_{ra}^\dagger(x)m + g_{la}C_{la}^\dagger(x)m$$
$$+ g_{rb}C_{rb}^\dagger(x)m + g_{lb}C_{lb}^\dagger(x)m] + \mathrm{H.c.}\},$$
(14)

where $C_{\alpha\beta}^\dagger(x)$ ($\alpha = r, l$ and $\beta = a, b$) is the corresponding creation operator of the photon of the βth waveguide and $g_{\alpha\beta}$ is the coupling strength between the GSE and the corresponding waveguide in different directions. The eigenstate of such a model is expanded as

$$|\Psi\rangle = \int dx[\Phi_{ra}(x)C_{ra}^\dagger(x) + \Phi_{la}(x)C_{la}^\dagger(x) + \Phi_{rb}(x)C_{rb}^\dagger(x)$$
$$+ \Phi_{lb}(x)C_{lb}^\dagger(x)]|\varnothing\rangle + u_m m^\dagger|\varnothing\rangle.$$
(15)

By applying the same method as before (see Appendix A for details), we can obtain the transmission amplitudes of different directions

$$t_{1\to3} = t_{4\to2} = -\frac{e^{-i\theta}(1+e^{i\theta})^2\sqrt{\Gamma_{ra}}\sqrt{\Gamma_{rb}}}{(1+e^{i\theta})(\Gamma_{la}+\Gamma_{lb}+\Gamma_{ra}+\Gamma_{rb})-i\tilde{\Delta}},$$
(16)

$$t_{3\to4} = 1 - \frac{e^{-i\theta}(1+e^{i\theta})^2\Gamma_{lb}}{(1+e^{i\theta})(\Gamma_{la}+\Gamma_{lb}+\Gamma_{ra}+\Gamma_{rb})-i\tilde{\Delta}},$$
(17)

$$t_{2\to1} = 1 - \frac{e^{-i\theta}(1+e^{i\theta})^2\Gamma_{la}}{(1+e^{i\theta})(\Gamma_{la}+\Gamma_{lb}+\Gamma_{ra}+\Gamma_{rb})-i\tilde{\Delta}},$$
(18)

$$t_{1\to2} = 1 - \frac{e^{-i\theta}(1+e^{i\theta})^2\Gamma_{ra}}{(1+e^{i\theta})(\Gamma_{la}+\Gamma_{lb}+\Gamma_{ra}+\Gamma_{rb})-i\tilde{\Delta}},$$
(19)

$$t_{2\to4} = t_{3\to1} = -\frac{e^{-i\theta}(1+e^{i\theta})^2\sqrt{\Gamma_{la}}\sqrt{\Gamma_{lb}}}{(1+e^{i\theta})(\Gamma_{la}+\Gamma_{lb}+\Gamma_{ra}+\Gamma_{rb})-i\tilde{\Delta}},$$
(20)

$$t_{4\to3} = 1 - \frac{e^{-i\theta}(1+e^{i\theta})^2\Gamma_{rb}}{(1+e^{i\theta})(\Gamma_{la}+\Gamma_{lb}+\Gamma_{ra}+\Gamma_{rb})-i\tilde{\Delta}},$$
(21)

where $\Gamma_{\alpha\beta} = g_{\alpha\beta}^2/v_g$ and $\theta = \theta_0 + \tau\Delta$.

We first focus on the perfect chiral case of $\Gamma_{la} = \Gamma_{lb} = \Gamma_l = 0$ and $\Gamma_{ra} = \Gamma_{rb} = \Gamma_r$ in the Markovian regime. From Eqs. (18) and (19) we can obtain $T_{2\to1} \equiv 1$ and the value of $T_{1\to2}$ can be modulated by the system parameters in the above perfect chiral condition, which also is observed in Figs. 9(a) and 9(b). The perfect nonreciprocity occurs when Δ is equal to the Lamb shift $\Delta_L = 2\Gamma_r \sin\theta_0$ under the current system parameters. Thereby, the single-photon diode behavior is extended to the double-waveguide system. Here the production of nonreciprocity no longer requires the participation of intrinsic dissipation of the magnon mode, i.e., $\gamma_m = 0$ since the existence of the waveguide b allows it to act as a channel to collect photons emitted by the GSE compared to the case of a single waveguide, which can be understood via the transmission spectrum $T_{1\to3}$. It is seen that $T_{1\to3}$ can reach 1 for $\Delta = \Delta_L$ due to the fact that the chiral magnon-photon coupling induces an imbalance between the photons emitted in the right and left directions of the waveguide b and blocks $T_{1\to4}$ to 0. Thereby, the photon input from port 1 of the waveguide a is completely routed to port 3 of another waveguide b rather than transmitted to port 2. Thus, $T_{1\to2}$ can be suppressed to 0 and the perfectly nonreciprocal transmission is achieved in the waveguide a. Meanwhile, one of the key components for constructing quantum networks, the single-photon targeted router, also can be actually realized in our work. The above interesting results support the design of a single-photon circulator.

Based on Eqs. (16)–(21), we show the transmission properties of a single photon in different directions. It can be found from Fig. 9(a) that $T_{3\to4} = T_{2\to1} \equiv 1$ in the whole frequency range and $T_{1\to3} = T_{4\to2} = 1$ at the effective resonance point $\Delta = \Delta_L$. This means that the photon input from port 2 or 3 decouples to the GSE and is directly output from port 1 or 4 due to the chiral magnon-photon interaction. Meanwhile, the photon input from port 1 or 4 can be routed to port 3 or 2 of another waveguide, which forms two single-photon targeted routers in different directions. By the above analysis, for a frequency $\omega = \omega_m + \Delta_L$, the directional single-photon transport in the forward-circulation direction $1 \to 3 \to 4 \to 2 \to 1$ is accomplished. However, the routing directions $T_{3\to1} = T_{2\to4} = 0$ at $\Delta = \Delta_L$, which implies the achievement of two nonreciprocal single-photon routers due to $T_{1\to3} = T_{4\to2} = 1$

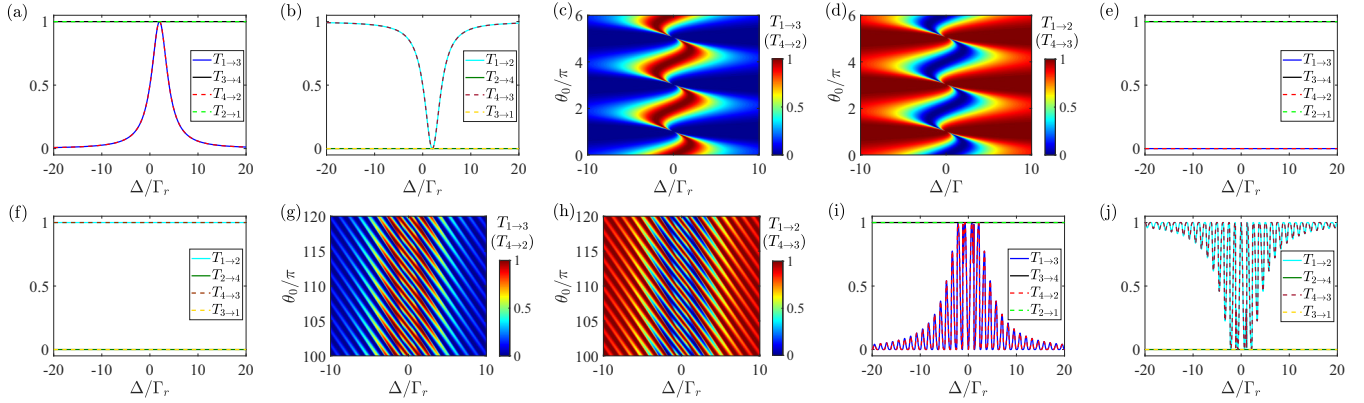FIG. 9. Transmission probability $T_{1\to3}$ from port 1 to port 3, transmission probability $T_{3\to4}$ from port 3 to port 4, transmission probability $T_{4\to2}$ from port 4 to port 2, and transmission probability $T_{2\to1}$ from port 2 to port 1 versus Δ for (a) $\theta_0 = \pi/2$ in the Markovian regime, (e) $\theta_0 = \pi$ in the Markovian regime, and (i) $\theta_0 = 105\pi$ in the non-Markovian regime. Also shown is the transmission probability $T_{1\to2}$ from port 1 to port 2, the transmission probability $T_{2\to4}$ from port 2 to port 4, the transmission probability $T_{4\to3}$ from port 4 to port 3, and the transmission probability $T_{3\to1}$ from port 3 to port 1 versus Δ for (b) $\theta_0 = \pi/2$ in the Markovian regime, (f) $\theta_0 = \pi$ in the Markovian regime, and (j) $\theta_0 = 105\pi$ in the non-Markovian regime. Here $T_{1\to3} = T_{4\to2}$ varies with Δ and θ_0 in (c) the Markovian regime and (g) the non-Markovian regime and $T_{1\to2} = T_{4\to3}$ varies with Δ and θ_0 in (d) the Markovian regime and (h) the non-Markovian regime. In (g)–(j) $\tau\Gamma_r = 5$. In addition, $\gamma_m = 0$, $\Gamma_{la} = \Gamma_{lb} = \Gamma_l = 0$, and $\Gamma_{ra} = \Gamma_{rb} = \Gamma_r$.

with the same frequency of the input photon. Also $T_{1\to2} = T_{4\to3} = 0$ is realized. Finally, the backward-circulation transport direction $1 \to 2 \to 4 \to 3 \to 1$ can be perfectly blocked [see Fig. 9(b)]. We obtain a high-performance directional magnon-based single-photon circulator. More importantly, it has a high tunability. The desired working frequency point of the single-photon circulator is obtained by appropriately adjusting the phase θ_0, which also is used to modulate periodically the operation frequency bandwidth due to $\Gamma_{\text{eff}} = \gamma_m + 2\Gamma_r(1 + \cos\theta_0)$, which can be clearly seen in Figs. 9(c) and 9(d). It is worth mentioning that the magnon mode in the GSE is obscured due to the destructive quantum interference for $\theta_0 = (2\xi + 1)\pi$, which gives rise to two single-photon targeted routers which are turned off, i.e., $T_{1\to3} = T_{4\to2} = 0$, and further causes the directional circulator to be shut down [see Figs. 9(e) and 9(f)]. Thus, θ_0 can be regarded as the controller of the work efficiency and the bandwidth of the single-photon circulator.

In the following, we turn our attention to the non-Markovian regime. Two single-photon targeted routers are strongly non-Markovian. From Fig. 9(g) it can be seen that the output spectra $T_{1\to3} = T_{4\to2}$ exhibit multiple-peak characteristics and they can simultaneously reach optimal routing probability 1 with multiple frequency points. Therefore, two multifrequency single-photon targeted routers are obtained. Meanwhile, $T_{3\to4} = T_{2\to1} \equiv 1$ still is achieved in the non-Markovian regime. The single-photon circulator along $1 \to 3 \to 4 \to 2 \to 1$ can work well at multiple frequency points with a narrow frequency band. The single-photon transport along $1 \to 2 \to 4 \to 3 \to 1$ simultaneously is prohibited since $T_{2\to4} = T_{3\to1} \equiv 0$ and $T_{1\to2} = T_{4\to3} = 0$ at the same multiple frequency points, as shown in Fig. 9(h). We also obtain a phase-modulated multiple-work-frequency single-photon circulator. In particular, in Figs. 9(i) and 9(j), non-Markovianity-induced nonreciprocity keeps the circulator working instead of closing for $\theta_0 = (2\xi + 1)\pi$, which

makes up for the deficiency of an unrealizable circulator under the same condition in the Markovian regime [see Figs. 9(e) and 9(f)]. With the chiral condition $\Gamma_{la} = \Gamma_{lb} = \Gamma_l$ and $\Gamma_{ra} = \Gamma_{rb} = \Gamma_r = 0$ (Fig. 10), we can obtain that the single-photon circulator in the direction $1 \to 2 \to 4 \to 3 \to$
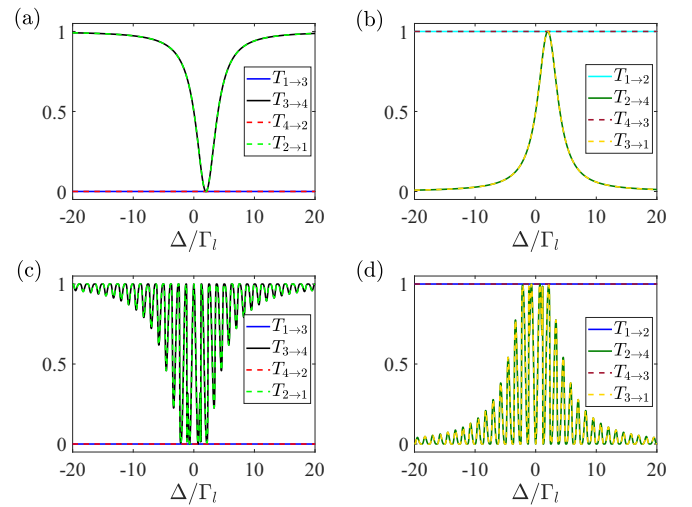

FIG. 10. Transmission probability $T_{1\to3}$ from port 1 to port 3, transmission probability $T_{3\to4}$ from port 3 to port 4, transmission probability $T_{4\to2}$ from port 4 to port 2, and transmission probability $T_{2\to1}$ from port 2 to port 1 versus Δ for (a) $\theta_0 = \pi/2$ in the Markovian regime and (c) $\theta_0 = 105\pi$ in the non-Markovian regime. Also shown is the transmission probability $T_{1\to2}$ from port 1 to port 2, the transmission probability $T_{2\to4}$ from port 2 to port 4, the transmission probability $T_{4\to3}$ from port 4 to port 3, and the transmission probability $T_{3\to1}$ from port 3 to port 1 versus Δ for (b) $\theta_0 = \pi/2$ in the Markovian regime and (d) $\theta_0 = 105\pi$ in the non-Markovian regime. Here $\Gamma_r = 0$, $\Gamma_l \neq 0$, and the other parameters are the same as in Fig. 9.

1 is completed. However, the opposite direction $1 \to 3 \to 4 \to 2 \to 1$ is prohibited. Therefore, single-photon circulators of different circulating directions can be regulated based on different chiral conditions. The non-Markovian characteristics of the single-photon circulator can still be achieved in such a circulating direction. Our results provide a possibility for realizing tunable multifrequency and narrow-operational-bandwidth quantum magnon devices.

IV. CONCLUSION

The nonreciprocal single-photon scattering behavior has been explored through the chiral interaction between the magnon mode in the GSE and the photon propagating in waveguides. We found that the synergy of the chiral magnon-photon coupling and intrinsic dissipation of magnon mode induces nonreciprocal transmission since they provide the conditions required for the implementation of nonreciprocity, i.e., the TRS breaking and non-Hermitian potential in the case of a single waveguide. The strength of nonreciprocity can be modulated flexibly by the accumulated phase of the propagating photon based on constructive and destructive interferences. In addition, we showed simultaneously the controlled single-photon transmission behavior in both the Markovian and non-Markovian regimes, which depends on whether the time-delay effect of a single photon propagating between two coupling points can be ignored. In the Markovian regime, the optimal nonreciprocity can be obtained for a single specific frequency point that is closely related to the Lamb shift and the bandwidth of realizing nonreciprocity is characterized by the effective decay rate. The interesting thing is that the property of multiple narrow, strongly nonreciprocal transmission windows occurs in the non-Markovian regime since the accumulated phase becomes detuning dependent. The multifrequency single-photon diode behavior is realized. In particular, when the GSE completely decouples to the waveguide due to the destructive interference in the Markovian regime, the transmissions in two input directions are always reciprocal. Non-Markovianity can make the GSE no longer decoupled from the waveguide and produce multiple-frequency strong nonreciprocity. Non-Markovianity-induced nonreciprocity is implemented. Moreover, the study of nonreciprocity was extended to the GSE-double waveguides system. This enabled the occurrence of nonreciprocity without the participation of intrinsic dissipation of the magnon mode since the second waveguide can act as a dissipation channel to collect the photon emitted by the GSE. The high-performance, narrow-operational-bandwidth, and multifrequency single-photon targeted router and circulator were designed based on this physical mechanism. The single-photon quantum devices have a high tunability; in particular, the circulating direction of the single-photon circulator can be regulated by adjusting the chiral coupling condition. In addition, our proposal may be easier to implement in practice since the realization and modulation of the GSE-waveguide setup have been shown to carry out at room temperature in experiment [59]. Our results provide powerful tools for controlling single-photon transport in the waveguide magnonics, which may promote further developments in the emerging quantum magnonics community and giant atom physics and

have potential applications in chiral quantum engineering and quantum information science [29,30,60].

APPENDIX A: DERIVATIONS OF THE TRANSMISSION PROBABILITY AMPLITUDES OF DIFFERENT DIRECTIONS IN THE GSE–DOUBLE-WAVEGUIDE SYSTEM

Submitting Eqs. (12)–(15) into $H|\Psi\rangle = \omega|\Psi\rangle$ leads to the expressions

$$-iv_g \frac{\partial}{\partial x}\Phi_{r\beta}(x) + g_{r\beta}u_m[\delta(x) + \delta(x - x_0)] = \omega\Phi_{r\beta}(x),$$
$$\text{(A1)}$$

$$iv_g \frac{\partial}{\partial x}\Phi_{l\beta}(x) + g_{l\beta}u_m[\delta(x) + \delta(x - x_0)] = \omega\Phi_{l\beta}(x), \quad \text{(A2)}$$

$$(\omega_m - i\gamma_m)u_m + \sum_{\alpha,\beta} g_{\alpha\beta}[\Phi_{\alpha\beta}(0) + \Phi_{\alpha\beta}(x_0)] = \omega u_m, \quad \text{(A3)}$$

where $\alpha = r, l$ and $\beta = a, b$. We assume that double waveguides have the same dispersion relation $\omega = kv_g$.

For different input directions, the wave functions of a single photon are expressed in the following forms [64,67,68,73]. For the case of single-photon input from port 1, they can be expressed as

$$\Phi_{ra}(x) = e^{ikx}[\Theta(-x) + A_a\Theta(x)\Theta(x_0 - x)$$
$$+ t_{1\to 2}\Theta(x - x_0)],$$

$$\Phi_{la}(x) = e^{-ikx}[t_{1\to 1}\Theta(-x) + B_a\Theta(x)\Theta(x_0 - x)],$$

$$\Phi_{rb}(x) = e^{ikx}[A_b\Theta(x)\Theta(x_0 - x) + t_{1\to 3}\Theta(x - x_0)],$$

$$\Phi_{lb}(x) = e^{-ikx}[t_{1\to 4}\Theta(-x) + B_b\Theta(x)\Theta(x_0 - x)]. \quad \text{(A4)}$$

For input from port 2, they can be described by

$$\Phi_{ra}(x) = e^{ikx}[t_{2\to 2}\Theta(x - x_0) + \tilde{A}_a\Theta(x)\Theta(x_0 - x)],$$

$$\Phi_{la}(x) = e^{-ikx}[\Theta(x - x_0) + \tilde{B}_a\Theta(x)\Theta(x_0 - x)$$
$$+ t_{2\to 1}\Theta(-x)], \quad \text{(A5)}$$

$$\Phi_{rb}(x) = e^{ikx}[t_{2\to 3}\Theta(x - x_0) + \tilde{A}_b\Theta(x)\Theta(x_0 - x)],$$

$$\Phi_{lb}(x) = e^{-ikx}[\tilde{B}_b\Theta(x)\Theta(x_0 - x) + t_{2\to 4}\Theta(-x)].$$

For input port 3, they have the forms

$$\Phi_{ra}(x) = e^{ikx}[t_{3\to 2}\Theta(x - x_0) + \tilde{A}'_a\Theta(x)\Theta(x_0 - x)],$$

$$\Phi_{la}(x) = e^{-ikx}[\tilde{B}'_a\Theta(x)\Theta(x_0 - x) + t_{3\to 1}\Theta(-x)],$$

$$\Phi_{rb}(x) = e^{ikx}[t_{3\to 3}\Theta(x - x_0) + \tilde{A}'_b\Theta(x)\Theta(x_0 - x)],$$

$$\Phi_{lb}(x) = e^{-ikx}[\Theta(x - x_0) + \tilde{B}'_b\Theta(x)\Theta(x_0 - x)$$
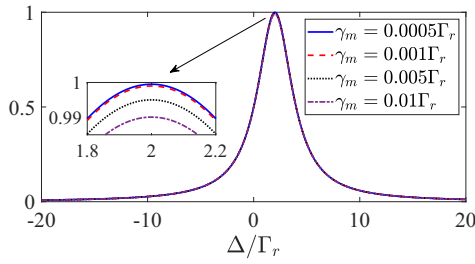$$+ t_{3\to 4}\Theta(-x)]. \quad \text{(A6)}$$

FIG. 11. Transmission probability $T_{1\to3}$ from port 1 to port 3 versus Δ for different γ_m/Γ_r. The other parameters are the same as in Fig. 9(a).

When the input direction is port 4, they read

$$\Phi_{ra}(x) = e^{ikx}[A'_a\Theta(x)\Theta(x_0 - x) + t_{4\to2}\Theta(x - x_0)],$$

$$\Phi_{la}(x) = e^{-ikx}[t_{4\to1}\Theta(-x) + B'_a\Theta(x)\Theta(x_0 - x)],$$

$$\Phi_{rb}(x) = e^{ikx}[\Theta(-x) + A'_b\Theta(x)\Theta(x_0 - x)$$
$$+ t_{4\to3}\Theta(x - x_0)],$$

$$\Phi_{lb}(x) = e^{-ikx}[t_{4\to4}\Theta(-x) + B'_b\Theta(x)\Theta(x_0 - x)]. \quad \text{(A7)}$$

Here $\mathbb{A}_\beta$ ($\mathbb{A} = A, \tilde{A}, \tilde{A}'$, and A') and $\mathbb{B}_\beta$ ($\mathbb{B} = B, \tilde{B}, \tilde{B}'$, and B') are the transport probability amplitudes of right-moving and left-moving photons in the βth waveguide with the region $0 < x < x_0$ for the photon input from different ports, respectively, and $t_{\mu\to\varsigma}$ ($\mu, \varsigma = 1, 2, 3, 4$) denotes the amplitude of photon transmission from port μ to port ς. Submitting Eqs. (A4)–(A7) into (A1)–(A3), the transmission probability amplitudes can be obtained in Eqs. (16)–(21).

APPENDIX B: EXPERIMENTAL IMPLEMENTATION

In this Appendix we discuss possible experimental implementation of our scheme. In the recent experiment of the GSE-waveguide system [59], the damping rate of the magnon mode emitted into the waveguide is $\Gamma \sim 0.8$ MHz and the intrinsic dissipation rate of the magnon mode is $\gamma_m/2\pi \sim 1.4$ MHz. Thus, $\gamma_m = 11\Gamma_r$ of our theoretical model is consistent with the parameters of the experiment. Furthermore, the damping rate of the magnon mode emitted into the waveguide can also be comparable to the intrinsic dissipation rate of the magnon mode in recent experiments [90,91] i.e., $\Gamma_r \sim \gamma_m$ is set in our work. The strong magnon-photon coupling has also been realized experimentally based on the waveguide magnonics system [45,57]. In particular, in the YIG sphere–coplanar waveguide coupling system [57], the magnon-photon coupling strength $g/2\pi = 130$ MHz and the intrinsic dissipation rate of the magnon mode $\gamma_m/2\pi = 1$ MHz are achieved. In this case, we can evaluate $\gamma_m/\Gamma \sim 0.001$ on the basis of $\Gamma = g^2/v_g$. These parameters of magnon-photon coupling also make it possible to achieve optimal nonreciprocity at different frequency points because the strongest nonreciprocity can be realized at $\Delta = \Delta_L = (\Gamma_l + \Gamma_r)\sin\theta_0$ and $\gamma_m = (\Gamma_l + \Gamma_r)(1 + \cos\theta_0)$. Taking the direction $T_{1\to3}$ of the targeted router as an example, we display the influence of γ_m/Γ_r on the property of single-photon routing in Fig. 11. It is found that γ_m/Γ_r only affects the routing efficiency and has a tiny effect in the strong magnon-photon

regime. Even though $\gamma_m/\Gamma_r = 0.01$, the routing efficiency can still reach 0.99. The routing efficiency is almost perfect based on the recent experimental parameter $\gamma_m/\Gamma_r \sim 0.001$ [57]. Our scheme is close to the actual system and may be completed experimentally.

For the chirality of the GSE-waveguide system, there is no experimental demonstration of the chiral coupling in our scheme. However, this may be inspired based on previous chiral magnon-photon coupling schemes [46,47,75–77,90,92]. Here we also propose an efficient scheme to implement the chiral GSE. Similar to recent schemes in theory [69–71] and experiment [72] for the realization of chiral giant atoms, we introduce the coupling phase ϕ of the magnon-photon scheme to the GSE-waveguide system, which may be achieved by applying a synthetic magnetic flux [96–100]. The Hamiltonian of the GSE-single waveguide system with the magnon-photon coupling phase ϕ can be given by

$$H_{wg} = -iv_g \int dx \left(C_r^\dagger(x)\frac{\partial}{\partial x}C_r(x) - C_l^\dagger(x)\frac{\partial}{\partial x}C_l(x) \right), \quad \text{(B1)}$$

$$H_m = (\omega_m - i\gamma_m)m^\dagger m, \quad \text{(B2)}$$

$$H_{int} = \int dx\{\delta(x)[ge^{i\phi}C_r^\dagger(x)m + ge^{i\phi}C_l^\dagger(x)m]$$
$$+ \delta(x - x_0)[gC_r^\dagger(x)m + gC_l^\dagger(x)m] + \text{H.c.}\}. \quad \text{(B3)}$$

Here the magnon-photon coupling phase ϕ is introduced at the coupling point $x_1 = 0$ and we set $x_2 = x_0$.

By applying the same method as above, we can obtain

$$t_{1\to2} = 1 - \frac{\Gamma[1 + \cos(\phi + \theta)]}{\Gamma(1 + e^{i\theta}\cos\phi) - i\tilde{\Delta}/2}, \quad \text{(B4)}$$

$$t_{2\to1} = 1 - \frac{\Gamma[1 + \cos(\phi - \theta)]}{\Gamma(1 + e^{i\theta}\cos\phi) - i\tilde{\Delta}/2}, \quad \text{(B5)}$$

where $\Gamma = g^2/v_g$. We can define the emission rates of the GSE in two input directions as [72] $\Gamma_{1\to2}/\Gamma = 1 + \cos(\phi + \theta)$ and $\Gamma_{2\to1}/\Gamma = 1 + \cos(\phi - \theta)$. In the Markovian regime, we set $\phi = \theta_0 = \pi/2$ and $\Gamma_{1\to2}/\Gamma_{2\to1} = 0$ is obtained, which shows the property of perfect chirality of magnon-photon coupling and is equivalent to the case of $\Gamma_r = 0$ in the main text. Thus, $T_{1\to2} \equiv 1$ and $T_{2\to1}$ is suppressed to 0 for the resonance photon [Fig. 12(a)]. The perfect nonreciprocity of single-photon transmission is realized. When the phases are tuned to $\phi = 3\pi/2$ and $\theta_0 = \pi/2$, $\Gamma_{2\to1}/\Gamma_{1\to2} = 0$, which corresponds to the case of $\Gamma_l = 0$; $T_{2\to1} \equiv 1$ and $T_{1\to2} = 0$ for $\Delta = 0$. We can also obtain the required strength of chirality by choosing appropriate values of the phases, which can be observed in Fig. 12(b), which shows that the chiral rate $\eta_d = \Gamma_{1\to2}/\Gamma_{2\to1}$ varies with phase ϕ. Thereby, the phase ϕ can further tune the nonreciprocal behavior of the single photon [Fig. 12(c)]. Furthermore, the coordinated modulation of two phases ϕ and θ_0 plays an important role in the regulation of the frequency point of achieving perfect nonreciprocity because the optimal nonreciprocity occurs at $\Delta = 2\Gamma\sin\theta_0\cos\phi$, as shown in Figs. 12(d) and 12(e).

The above phenomena can be better understood from the perspective of magnon excitation. The amplitudes of magnon
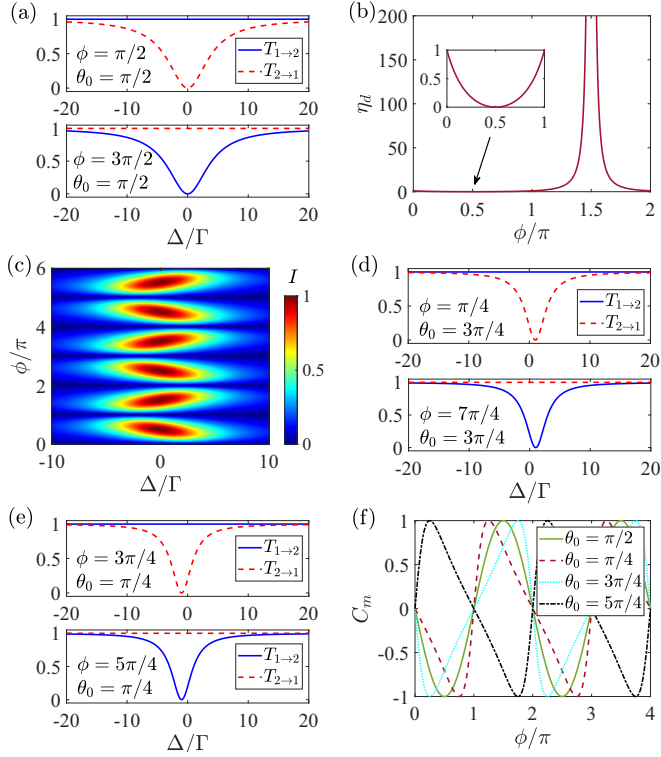
FIG. 12. (a), (d), and (e) Transmission probability $T_{1\to2}$ from port 1 to port 2 and transmission probability $T_{2\to1}$ from port 2 to port 1 versus Δ for different the values of the phases ϕ and θ_0. (b) Chiral rate η_d versus ϕ for $\theta_0 = \pi/2$. (c) Isolation ratio I varying with Δ and ϕ for $\theta_0 = \pi/2$. (f) Contrast ratio C_m of magnon excitation of two input directions versus ϕ for different values of θ_0. In addition, (a) and (c) $\gamma_m = 2\Gamma$ and (d) and (e) $\gamma_m = \Gamma$.

excitations of different input directions can be given by

$$u_{m1\to2} = -\frac{ig[1 + e^{i(\phi+\theta)}]}{\Gamma[e^{i\theta} + 2e^{i\phi} + e^{i(\theta+2\phi)}] - i\tilde{\Delta}e^{i\phi}}, \quad (B6)$$

$$u_{m2\to1} = -\frac{ig[1 + e^{i(\phi-\theta)}]}{\Gamma[e^{i\theta} + 2e^{i\phi} + e^{i(\theta+2\phi)}] - i\tilde{\Delta}e^{i\phi}}. \quad (B7)$$

The contrast ratio C_m of magnon excitations of two input directions is defined as $C_m = (|u_{m1\to2}|^2 - |u_{m2\to1}|^2)/(|u_{m1\to2}|^2 + |u_{m2\to1}|^2)$. From Fig. 12(f) it can be seen that $C_m = 0$ when $\phi = \xi\pi$, which implies that the photon input from two directions can cause the same magnon excitation, which corresponds to the case of nonchirality. Thus, single-photon transmission is reciprocal. When $\phi + \theta_0 = (2\xi + 1)\pi$, $C_m = -1$ is realized. This indicates that the magnon mode m only interacts with the photon input from port 2 and decouples with the photon input from port 1. For the case of $\phi - \theta_0 = (2\xi + 1)\pi$, $C_m = 1$ suggests that only photon input from port 1 interacts with the magnon mode m. Here $C_m = \pm 1$ is equivalent to a perfectly chiral magnon-photon coupling effect in the waveguide magnonics system [46,47,92]. For the case of $0 < |C_m| < 1$ which can be implemented by tuning the phases ϕ and θ_0, the magnon-photon coupling is imperfect chirality. The coordinated modulation of two phases can complete the different strength of chirality of the system. The above

discussion demonstrates that the phases can be responsible for the modulation of chirality of the GSE-waveguide system and further control nonreciprocity.

For the GSE–double-waveguide system, we can introduce simultaneously the phase ϕ at the coupling point $x = 0$ ($x_1 = x_4 = 0$) of each waveguide and the GSE. We set $x_2 = x_3 = x_0$. The Hamiltonian of such a system is expressed as

$$H_{\text{wg}} = -iv_g \int dx \left(C_{ra}^\dagger(x) \frac{\partial}{\partial x} C_{ra}(x) - C_{la}^\dagger(x) \frac{\partial}{\partial x} C_{la}(x) \right)$$
$$- iv_g \int dx \left(C_{rb}^\dagger(x) \frac{\partial}{\partial x} C_{rb}(x) - C_{lb}^\dagger(x) \frac{\partial}{\partial x} C_{lb}(x) \right), \quad (B8)$$

$$H_{\text{m}} = (\omega_m - i\gamma_m)m^\dagger m, \quad (B9)$$

$$H_{\text{int}} = \int dx\{\delta(x)[g_a e^{i\phi} C_{ra}^\dagger(x)m + g_a e^{i\phi} C_{la}^\dagger(x)m$$
$$+ g_b e^{i\phi} C_{rb}^\dagger(x)m + g_b e^{i\phi} C_{lb}^\dagger(x)m]$$
$$+ \delta(x - x_0)[g_a C_{ra}^\dagger(x)m + g_a C_{la}^\dagger(x)m$$
$$+ g_b C_{rb}^\dagger(x)m + g_b C_{lb}^\dagger(x)m] + \text{H.c.}\}. \quad (B10)$$

By using the same method as above, the corresponding transmission amplitudes can be obtained as

$$t_{1\to3} = t_{4\to2} = -\frac{e^{-i\theta}[1 + e^{i(\theta+\phi)}]^2 \sqrt{\Gamma_a \Gamma_b}}{[e^{i\theta} + 2e^{i\phi} + e^{i(\theta+2\phi)}](\Gamma_a + \Gamma_b) - i\tilde{\Delta}e^{i\phi}}, \quad (B11)$$

$$t_{3\to4} = 1 - \frac{[1 + e^{i(\phi-\theta)}](e^{i\theta} + e^{i\phi})\Gamma_b}{[e^{i\theta} + 2e^{i\phi} + e^{i(\theta+2\phi)}](\Gamma_a + \Gamma_b) - i\tilde{\Delta}e^{i\phi}}, \quad (B12)$$

$$t_{2\to1} = 1 - \frac{[1 + e^{i(\phi-\theta)}](e^{i\theta} + e^{i\phi})\Gamma_a}{[e^{i\theta} + 2e^{i\phi} + e^{i(\theta+2\phi)}](\Gamma_a + \Gamma_b) - i\tilde{\Delta}e^{i\phi}}, \quad (B13)$$

$$t_{1\to2} = 1 - \frac{[1 + e^{i(\phi+\theta)}](e^{-i\theta} + e^{i\phi})\Gamma_a}{[e^{i\theta} + 2e^{i\phi} + e^{i(\theta+2\phi)}](\Gamma_a + \Gamma_b) - i\tilde{\Delta}e^{i\phi}}, \quad (B14)$$

$$t_{2\to4} = t_{3\to1} = -\frac{[1 + e^{i(\phi-\theta)}](e^{i\theta} + e^{i\phi})\sqrt{\Gamma_a \Gamma_b}}{[e^{i\theta} + 2e^{i\phi} + e^{i(\theta+2\phi)}](\Gamma_a + \Gamma_b) - i\tilde{\Delta}e^{i\phi}}, \quad (B15)$$

$$t_{4\to3} = 1 - \frac{[1 + e^{i(\phi+\theta)}](e^{-i\theta} + e^{i\phi})\Gamma_b}{[e^{i\theta} + 2e^{i\phi} + e^{i(\theta+2\phi)}](\Gamma_a + \Gamma_b) - i\tilde{\Delta}e^{i\phi}}. \quad (B16)$$

Here $\Gamma_a = g_a^2/v_g$ and $\Gamma_b = g_b^2/v_g$. We set $\Gamma_a = \Gamma_b = \Gamma$ in the following. The transmission spectra of different directions, based on the above equations, are exhibited in Figs. 13(a) and 13(b). Obviously, the high-efficiency single-photon targeted router and circulator are implemented. In addition, the coor-
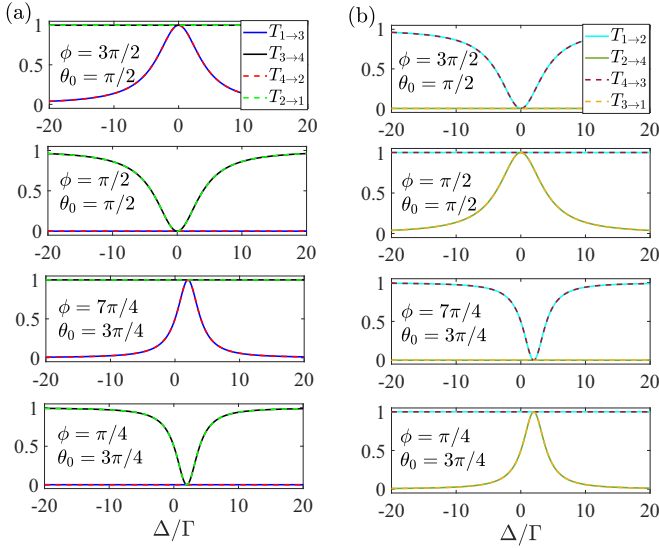
FIG. 13. (a) Transmission probability $T_{1\to3}$ from port 1 to port 3, transmission probability $T_{3\to4}$ from port 3 to port 4, transmission probability $T_{4\to2}$ from port 4 to port 2, and transmission probability $T_{2\to1}$ from port 2 to port 1 versus Δ for different the values of the phases ϕ and θ_0. (b) Also shown is the transmission probability $T_{1\to2}$ from port 1 to port 2, the transmission probability $T_{2\to4}$ from port 2 to port 4, the transmission probability $T_{4\to3}$ from port 4 to port 3, and the transmission probability $T_{3\to1}$ from port 3 to port 1 versus Δ for different values of the phases ϕ and θ_0. Here $\gamma_m = 0.001\Gamma$.

dinated modulations of two phases can control the operating frequency point of the targeted router and circulator and the
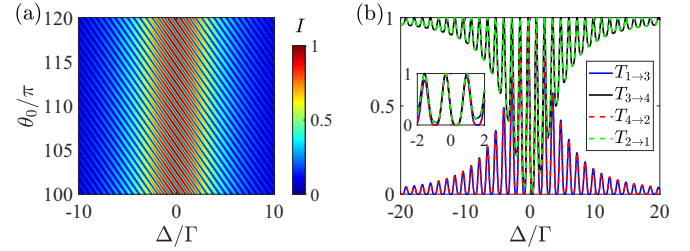

FIG. 14. (a) Isolation depth I varying with Δ and θ_0 for $\phi = \pi/2$ and $\tau\Gamma = 5$. (b) Transmission probability $T_{1\to3}$ from port 1 to port 3, transmission probability $T_{3\to4}$ from port 3 to port 4, transmission probability $T_{4\to2}$ from port 4 to port 2, and transmission probability $T_{2\to1}$ from port 2 to port 1 versus Δ when $\phi = 3\pi/2$, $\theta_0 = 105\pi$, and $\tau\Gamma = 5$. The other parameters in (a) are the same as in Fig. 12(a) and the other parameters in (b) are the same as Fig. 13(a).

routing and circulating directions. We can obtain the spectra that are consistent with Figs. 9 and 10 by adjusting the phases in the Markovian regime. In the non-Markovian regime, from Fig. 14 we can find that there are non-Markovian characteristics similar to those in the main text. Multiple narrow nonreciprocal transmission windows are also observed in the case of a single waveguide. The high-efficiency and tunable multifrequency single-photon targeted router and circulator with narrow operational bandwidth are also achieved. In conclusion, the strongly chiral GSE-waveguide system may be realized experimentally by introducing the magnon-photon coupling phase.

[1] D. Roy, C. M. Wilson, and O. Firstenberg, *Colloquium*: Strongly interacting photons in one-dimensional continuum, Rev. Mod. Phys. **89**, 021001 (2017).

[2] M. Arcari, I. Söllner, A. Javadi, S. Lindskov Hansen, S. Mahmoodian, J. Liu, H. Thyrrestrup, E. H. Lee, J. D. Song, S. Stobbe, and P. Lodahl, Near-unity coupling efficiency of a quantum emitter to a photonic crystal waveguide, Phys. Rev. Lett. **113**, 093603 (2014).

[3] J. S. Douglas, H. Habibian, C.-L. Hung, A. V. Gorshkov, H. J. Kimble, and D. E. Chang, Quantum many-body models with cold atoms coupled to photonic crystals, Nat. Photon. **9**, 326 (2015).

[4] A. Wallraff, D. I. Schuster, A. Blais, L. Frunzio, R.-S. Huang, J. Majer, S. Kumar, S. M. Girvin, and R. J. Schoelkopf, Strong coupling of a single photon to a superconducting qubit using circuit quantum electrodynamics, Nature (London) **431**, 162 (2004).

[5] L. Zhou, Z. R. Gong, Y.-x. Liu, C. P. Sun, and F. Nori, Controllable scattering of a single photon inside a one-dimensional resonator waveguide, Phys. Rev. Lett. **101**, 100501 (2008).

[6] J. Q. You and F. Nori, Atomic physics and quantum optics using superconducting circuits, Nature (London) **474**, 589 (2011).

[7] G. Andersson, B. Suri, L. Guo, T. Aref, and P. Delsing, Non-exponential decay of a giant artificial atom, Nat. Phys. **15**, 1123 (2019).

[8] B. Kannan, M. J. Ruckriegel, D. L. Campbell, A. F. Kockum, J. Braumüller, D. K. Kim, M. Kjaergaard, P. Krantz, A. Melville, B. M. Niedzielski, A. Vepsäläinen, R. Winik, J. L. Yoder, F. Nori, T. P. Orlando, S. Gustavsson, and W. D. Oliver, Waveguide quantum electrodynamics with superconducting artificial giant atoms, Nature (London) **583**, 775 (2020).

[9] A. M. Vadiraj, A. Ask, T. G. McConkey, I. Nsanzineza, C. W. S. Chang, A. F. Kockum, and C. M. Wilson, Engineering the level structure of a giant artificial atom in waveguide quantum electrodynamics, Phys. Rev. A **103**, 023710 (2021).

[10] A. González-Tudela, C. S. Muñoz, and J. I. Cirac, Engineering and harnessing giant atoms in high-dimensional baths: A proposal for implementation with cold atoms, Phys. Rev. Lett. **122**, 203603 (2019).

[11] L. Du, Y. Zhang, J.-H. Wu, A. F. Kockum, and Y. Li, Giant atoms in a synthetic frequency dimension, Phys. Rev. Lett. **128**, 223602 (2022).

[12] A. F. Kockum, P. Delsing, and G. Johansson, Designing frequency-dependent relaxation rates and Lamb shifts for a giant artificial atom, Phys. Rev. A **90**, 013837 (2014).

[13] L. Guo, A. Grimsmo, A. F. Kockum, M. Pletyukhov, and G. Johansson, Giant acoustic atom: A single quantum system with a deterministic time delay, Phys. Rev. A **95**, 053821 (2017).

[14] S. Longhi, Photonic simulation of giant atom decay, Opt. Lett. **45**, 3017 (2020).

[15] A. F. Kockum, G. Johansson, and F. Nori, Decoherence-free interaction between giant atoms in waveguide quantum electrodynamics, Phys. Rev. Lett. **120**, 140404 (2018).

[16] A. Carollo, D. Cilluffo, and F. Ciccarello, Mechanism of decoherence-free coupling between giant atoms, Phys. Rev. Res. **2**, 043184 (2020).

[17] L. Du, L. Guo, and Y. Li, Complex decoherence-free interactions between giant atoms, Phys. Rev. A **107**, 023705 (2023).

[18] S. L. Feng and W. Z. Jia, Manipulating single-photon transport in a waveguide-QED structure containing two giant atoms, Phys. Rev. A **104**, 063712 (2021).

[19] C. Wang, X.-S. Ma, and M.-T. Cheng, Giant atom-mediated single photon routing between two waveguides, Opt. Express **29**, 40116 (2021).

[20] X.-L. Yin, Y.-H. Liu, J.-F. Huang, and J.-Q. Liao, Single-photon scattering in a giant-molecule waveguide-QED system, Phys. Rev. A **106**, 013715 (2022).

[21] Y. T. Zhu, S. Xue, R. B. Wu, W. L. Li, Z. H. Peng, and M. Jiang, Spatial-nonlocality-induced non-Markovian electromagnetically induced transparency in a single giant atom, Phys. Rev. A **106**, 043710 (2022).

[22] L. Guo, A. F. Kockum, F. Marquardt, and G. Johansson, Oscillating bound states for a giant atom, Phys. Rev. Res. **2**, 043014 (2020).

[23] W. Zhao and Z. Wang, Single-photon scattering and bound states in an atom-waveguide system with two or multiple coupling points, Phys. Rev. A **101**, 053855 (2020).

[24] H. Xiao, L. Wang, Z.-H. Li, X. Chen, and L. Yuan, Bound state in a giant atom-modulated resonators system, npj Quantum Inf. **8**, 80 (2022).

[25] Q.-Y. Qiu, Y. Wu, and X.-Y. Lü, Collective radiance of giant atoms in non-Markovian regime, Sci. China Phys. Mech. Astron. **66**, 224212 (2023).

[26] H. Yu, Z. Wang, and J.-H. Wu, Entanglement preparation and nonreciprocal excitation evolution in giant atoms by controllable dissipation and coupling, Phys. Rev. A **104**, 013720 (2021).

[27] X.-L. Yin, W.-B. Luo, and J.-Q. Liao, Non-Markovian disentanglement dynamics in double-giant-atom waveguide-QED systems, Phys. Rev. A **106**, 063703 (2022).

[28] A. C. Santos and R. Bachelard, Generation of maximally entangled long-lived states with giant atoms in a waveguide, Phys. Rev. Lett. **130**, 053601 (2023).

[29] H. Y. Yuan, Y. Cao, A. Kamra, R. A. Duine, and P. Yan, Quantum magnonics: When magnon spintronics meets quantum information science, Phys. Rep. **965**, 1 (2022).

[30] B. Z. Rameshti, S. V. Kusminskiy, J. A. Haigh, K. Usami, D. Lachance-Quirion, Y. Nakamura, C.-M. Hu, H. X. Tang, G. E. W. Bauer, and Y. M. Blanter, Cavity magnonics, Phys. Rep. **979**, 1 (2022).

[31] Y. Tabuchi, S. Ishino, T. Ishikawa, R. Yamazaki, K. Usami, and Y. Nakamura, Hybridizing ferromagnetic magnons and microwave photons in the quantum limit, Phys. Rev. Lett. **113**, 083603 (2014).

[32] X. Zhang, C.-L. Zou, L. Jiang, and H. X. Tang, Strongly coupled magnons and cavity microwave photons, Phys. Rev. Lett. **113**, 156401 (2014).

[33] M. Goryachev, W. G. Farr, D. L. Creedon, Y. Fan, M. Kostylev, and M. E. Tobar, High-cooperativity cavity QED with magnons at microwave frequencies, Phys. Rev. Appl. **2**, 054002 (2014).

[34] A. Osada, R. Hisatomi, A. Noguchi, Y. Tabuchi, R. Yamazaki, K. Usami, M. Sadgrove, R. Yalla, M. Nomura, and Y. Nakamura, Cavity optomagnonics with spin-orbit coupled photons, Phys. Rev. Lett. **116**, 223601 (2016).

[35] X. Zhang, N. Zhu, C.-L. Zou, and H. X. Tang, Optomagnonic whispering gallery microresonators, Phys. Rev. Lett. **117**, 123605 (2016).

[36] H. Xie, L.-W. He, X. Shang, G.-W. Lin, and X.-M. Lin, Nonreciprocal photon blockade in cavity optomagnonics, Phys. Rev. A **106**, 053707 (2022).

[37] Y. Tabuchi, S. Ishino, A. Noguchi, T. Ishikawa, R. Yamazaki, K. Usami, and Y. Nakamura, Coherent coupling between a ferromagnetic magnon and a superconducting qubit, Science **349**, 405 (2015).

[38] X. Li, X. Wang, Z. Wu, W.-X. Yang, and A. Chen, Tunable magnon antibunching in a hybrid ferromagnet-superconductor system with two qubits, Phys. Rev. B **104**, 224434 (2021).

[39] D. Xu, X.-K. Gu, H.-K. Li, Y.-C. Weng, Y.-P. Wang, J. Li, H. Wang, S.-Y. Zhu, and J. Q. You, Quantum control of a single magnon in a macroscopic spin system, Phys. Rev. Lett. **130**, 193603 (2023).

[40] X. Zhang, C.-L. Zou, L. Jiang, and H. X. Tang, Cavity magnomechanics, Sci. Adv. **2**, e1501286 (2016).

[41] J. Li, S.-Y. Zhu, and G. S. Agarwal, Magnon-photon-phonon entanglement in cavity magnomechanics, Phys. Rev. Lett. **121**, 203601 (2018).

[42] J. Li and S. Gröblacher, Entangling the vibrational modes of two massive ferromagnetic spheres using cavity magnomechanics, Quantum Sci. Technol. **6**, 024005 (2021).

[43] R.-C. Shen, J. Li, Z.-Y. Fan, Y.-P. Wang, and J. Q. You, Mechanical bistability in Kerr-modified cavity magnomechanics, Phys. Rev. Lett. **129**, 123601 (2022).

[44] B. M. Yao, Y. S. Gui, Y. Xiao, H. Guo, X. S. Chen, W. Lu, C. L. Chien, and C.-M. Hu, Theory and experiment on cavity magnon-polariton in the one-dimensional configuration, Phys. Rev. B **92**, 184407 (2015).

[45] B. Yao, T. Yu, Y. S. Gui, J. W. Rao, Y. T. Zhao, W. Lu, and C.-M. Hu, Coherent control of magnon radiative damping with local photon states, Commun. Phys. **2**, 161 (2019).

[46] T. Yu, Y.-X. Zhang, S. Sharma, X. Zhang, Y. M. Blanter, and G. E. W. Bauer, Magnon accumulation in chirally coupled magnets, Phys. Rev. Lett. **124**, 107202 (2020).

[47] T. Yu, X. Zhang, S. Sharma, Y. M. Blanter, and G. E. W. Bauer, Chiral coupling of magnons in waveguides, Phys. Rev. B **101**, 094414 (2020).

[48] J. W. Rao, Y. P. Wang, Y. Yang, T. Yu, Y. S. Gui, X. L. Fan, D. S. Xue, and C.-M. Hu, Interactions between a magnon mode and a cavity photon mode mediated by traveling photons, Phys. Rev. B **101**, 064404 (2020).

[49] Y. Wang, W. Xiong, Z. Xu, G.-Q. Zhang, and J.-Q. You, Dissipation-induced nonreciprocal magnon blockade in a magnon-based hybrid system, Sci. China Phys. Mech. Astron. **65**, 260314 (2022).

[50] N. Zhu, X. Zhang, X. Han, C.-L. Zou, C. Zhong, C.-H. Wang, L. Jiang, and H. X. Tang, Waveguide cavity optomagnonics for microwave-to-optics conversion, Optica **7**, 1291 (2020).

[51] C.-Z. Chai, Z. Shen, Y.-L. Zhang, H.-Q. Zhao, G.-C. Guo, C.-L. Zou, and C.-H. Dong, Single-sideband microwave-to-optical conversion in high-Q ferrimagnetic microspheres, Photon. Res. **10**, 820 (2022).

[52] M. T. Kaffash, D. Wagle, A. Rai, T. Meyer, J. Q. Xiao, and M. B. Jungfleisch, Direct probing of strong magnon-photon coupling in a planar geometry, Quantum Sci. Technol. **8**, 01LT02 (2023).

[53] Z.-X. Liu and Y.-Q. Li, Optomagnonic frequency combs, Photon. Res. **10**, 2786 (2022).

[54] X. Wang, K.-W. Huang, Q.-Y. Qiu, and H. Xiong, Nonreciprocal double-carrier frequency combs in cavity magnonics, Chaos Soliton. Fract. **176**, 114137 (2023).

[55] H. Xiong, Magnonic frequency combs based on the resonantly enhanced magnetostrictive effect, Fund. Res. **3**, 8 (2023).

[56] F.-X. Sun, S.-S. Zheng, Y. Xiao, Q. Gong, Q. He, and K. Xia, Remote generation of magnon Schrödinger cat state via magnon-photon entanglement, Phys. Rev. Lett. **127**, 087203 (2021).

[57] Y. Li, V. G. Yefremenko, M. Lisovenko, C. Trevillian, T. Polakovic, T. W. Cecil, P. S. Barry, J. Pearson, R. Divan, V. Tyberkevych, C. L. Chang, U. Welp, W. K. Kwok, and V. Novosad, Coherent coupling of two remote magnonic resonators mediated by superconducting circuits, Phys. Rev. Lett. **128**, 047701 (2022).

[58] W.-J. Wu, Y.-P. Wang, J.-Z. Wu, J. Li, and J. Q. You, Remote magnon entanglement between two massive ferrimagnetic spheres via cavity optomagnonics, Phys. Rev. A **104**, 023711 (2021).

[59] Z.-Q. Wang, Y.-P. Wang, J. Yao, R.-C. Shen, W.-J. Wu, J. Qian, J. Li, S.-Y. Zhu, and J. Q. You, Giant spin ensembles in waveguide magnonics, Nat. Commun. **13**, 7580 (2022).

[60] P. Lodahl, S. Mahmoodian, S. Stobbe, A. Rauschenbeutel, P. Schneeweiss, J. Volz, H. Pichler, and P. Zoller, Chiral quantum optics, Nature (London) **541**, 473 (2017).

[61] M. Scheucher, A. Hilico, E. Will, J. Volz, and A. Rauschenbeutel, Quantum optical circulator controlled by a single chirally coupled atom, Science **354**, 1577 (2016).

[62] K. Xia, F. Nori, and M. Xiao, Cavity-free optical isolators and circulators using a chiral cross-Kerr nonlinearity, Phys. Rev. Lett. **121**, 203602 (2018).

[63] C.-H. Yan, Y. Li, H. Yuan, and L. F. Wei, Targeted photonic routers with chiral photon-atom interactions, Phys. Rev. A **97**, 023821 (2018).

[64] W.-B. Yan, W.-Y. Ni, J. Zhang, F.-Y. Zhang, and H. Fan, Tunable single-photon diode by chiral quantum physics, Phys. Rev. A **98**, 043852 (2018).

[65] X. Wang, W.-X. Yang, A.-X. Chen, L. Li, T. Shui, X. Li, and Z. Wu, Phase-modulated single-photon nonreciprocal transport and directional router in a waveguide-cavity-emitter system beyond the chiral coupling, Quantum Sci. Technol. **7**, 015025 (2022).

[66] D.-W. Liu, K.-W. Huang, Y. Wu, and L.-G. Si, Parametric amplification induced giant nonreciprocal unconventional photon blockade in a single microring resonator, Appl. Phys. Lett. **123**, 061103 (2023).

[67] Y. You, Y. Hu, G. Lin, Y. Qi, Y. Niu, and S. Gong, Quantum nonreciprocity based on electromagnetically induced transparency in chiral quantum-optical systems, Phys. Rev. A **103**, 063706 (2021).

[68] L. Du, Y.-T. Chen, and Y. Li, Nonreciprocal frequency conversion with chiral Λ-type atoms, Phys. Rev. Res. **3**, 043226 (2021).

[69] X. Wang and H.-R. Li, Chiral quantum network with giant atoms, Quantum Sci. Technol. **7**, 035007 (2022).

[70] A. Soro and A. F. Kockum, Chiral quantum optics with giant atoms, Phys. Rev. A **105**, 023712 (2022).

[71] Y.-T. Chen, L. Du, L. Guo, Z. Wang, Y. Zhang, Y. Li, and J.-H. Wu, Nonreciprocal and chiral single-photon scattering for giant atoms, Commun. Phys. **5**, 215 (2022).

[72] C. Joshi, F. Yang, and M. Mirhosseini, Resonance fluorescence of a chiral artificial atom, Phys. Rev. X **13**, 021039 (2023).

[73] J. Zhou, X.-L. Yin, and J.-Q. Liao, Chiral and nonreciprocal single-photon scattering in a chiral-giant-molecule waveguide-QED system, Phys. Rev. A **107**, 063703 (2023).

[74] X. Wang, T. Liu, A. F. Kockum, H.-R. Li, and F. Nori, Tunable chiral bound states with giant atoms, Phys. Rev. Lett. **126**, 043602 (2021).

[75] X. Zhang, A. Galda, X. Han, D. Jin, and V. M. Vinokur, Broadband nonreciprocity enabled by strong coupling of magnons and microwave photons, Phys. Rev. Appl. **13**, 044039 (2020).

[76] J. Bourhill, W. Yu, V. Vlaminck, G. E. W. Bauer, G. Ruoso, and V. Castel, Generation of circulating cavity magnon polaritons, Phys. Rev. Appl. **19**, 014030 (2023).

[77] H. Zhan, L. Sun, and H. Tan, Chirality-induced one-way quantum steering between two waveguide-mediated ferrimagnetic microspheres, Phys. Rev. B **106**, 104432 (2022).

[78] Y.-P. Wang, J. W. Rao, Y. Yang, P.-C. Xu, Y. S. Gui, B. M. Yao, J. Q. You, and C.-M. Hu, Nonreciprocity and unidirectional invisibility in cavity magnonics, Phys. Rev. Lett. **123**, 127202 (2019).

[79] B. Li, R. Huang, X. Xu, A. Miranowicz, and H. Jing, Nonreciprocal unconventional photon blockade in a spinning optomechanical system, Photon. Res. **7**, 630 (2019).

[80] N. Zhu, X. Han, C.-L. Zou, M. Xu, and H. X. Tang, Magnon-photon strong coupling for tunable microwave circulators, Phys. Rev. A **101**, 043842 (2020).

[81] Y. Xu, J.-Y. Liu, W. Liu, and Y.-F. Xiao, Nonreciprocal phonon laser in a spinning microwave magnomechanical system, Phys. Rev. A **103**, 053501 (2021).

[82] C. Zhao, R. Peng, Z. Yang, S. Chao, C. Li, Z. Wang, and L. Zhou, Nonreciprocal amplification in a cavity magnonics system, Phys. Rev. A **105**, 023709 (2022).

[83] Y.-L. Ren, S.-L. Ma, J.-K. Xie, X.-K. Li, M.-T. Cao, and F.-L. Li, Nonreciprocal single-photon quantum router, Phys. Rev. A **105**, 013711 (2022).

[84] K.-W. Huang, Y. Wu, and L.-G. Si, Parametric-amplification-induced nonreciprocal magnon laser, Opt. Lett. **47**, 3311 (2022).

[85] X. Wang, K.-W. Huang, and H. Xiong, Nonreciprocal sideband responses in a spinning microwave magnomechanical system, Opt. Express **31**, 5492 (2023).

[86] X. Huang, C. Lu, C. Liang, H. Tao, and Y.-C. Liu, Loss-induced nonreciprocity, Light Sci. Appl. **10**, 30 (2021).

[87] F. Roccati, S. Lorenzo, G. Calajò, G. M. Palma, A. Carollo, and F. Ciccarello, Exotic interactions mediated by a non-Hermitian photonic bath, Optica **9**, 565 (2022).

[88] J.-T. Shen and S. Fan, Theory of single-photon transport in a single-mode waveguide. I. Coupling to a cavity containing a two-level atom, Phys. Rev. A **79**, 023837 (2009).

[89] J.-T. Shen and S. Fan, Theory of single-photon transport in a single-mode waveguide. II. Coupling to a whispering-gallery-resonator containing a two-level atom, Phys. Rev. A **79**, 023838 (2009).

[90] Y. Han, C. Meng, H. Pan, J. Qian, Z. Rao, L. Zhu, Y. Gui, C.-M. Hu, and Z. An, Bound chiral magnonic polariton states for ideal microwave isolation, Sci. Adv. **9**, eadg4730 (2023).

[91] J. Qian, C. H. Meng, J. W. Rao, Z. J. Rao, Z. An, Y. Gui, and C.-M. Hu, Non-Hermitian control between absorption and transparency in perfect zero-reflection magnonics, Nat. Commun. **14**, 3437 (2023).

[92] T. Yu, Z. Luo, and G. E. W. Bauer, Chirality as generalized spin-orbit interaction in spintronics, Phys. Rep. **1009**, 1 (2023).

[93] X. Q. Li, X. Z. Zhang, G. Zhang, and Z. Song, Asymmetric transmission through a flux-controlled non-Hermitian scattering center, Phys. Rev. A **91**, 032101 (2015).

[94] H. Pichler and P. Zoller, Photonic circuits with time delays and quantum feedback, Phys. Rev. Lett. **116**, 093601 (2016).

[95] P. O. Guimond, M. Pletyukhov, H. Pichler, and P. Zoller, Delayed coherent quantum feedback from a scattering theory and a matrix product state perspective, Quantum Sci. Technol. **2**, 044012 (2017).

[96] L. D. Tzuang, K. Fang, P. Nussenzveig, S. Fan, and M. Lipson, Non-reciprocal phase shift induced by an effective magnetic flux for light, Nat. Photon. **8**, 701 (2014).

[97] K. Fang, J. Luo, A. Metelmann, M. H. Matheny, F. Marquardt, A. A. Clerk, and O. Painter, Generalized nonreciprocity in an optomechanical circuit via synthetic magnetism and reservoir engineering, Nat. Phys. **13**, 465 (2017).

[98] P. Roushan, C. Neill, A. Megrant, Y. Chen, R. Babbush, R. Barends, B. Campbell, Z. Chen, B. Chiaro, A. Dunsworth, A. Fowler, E. Jeffrey, J. Kelly, E. Lucero, J. Mutus, P. J. J. O'Malley, M. Neeley, C. Quintana, D. Sank, A. Vainsencher *et al.*, Chiral ground-state currents of interacting photons in a synthetic magnetic field, Nat. Phys. **13**, 146 (2017).

[99] C. W. Peterson, W. A. Benalcazar, M. Lin, T. L. Hughes, and G. Bahl, Strong nonreciprocity in modulated resonator chains through synthetic electric and magnetic fields, Phys. Rev. Lett. **123**, 063901 (2019).

[100] X.-W. Xu, Y. Li, B. Li, H. Jing, and A.-X. Chen, Nonreciprocity via nonlinearity and synthetic magnetism, Phys. Rev. Appl. **13**, 044070 (2020).